JOURNAL OF GLACIOLOGY

CAMBRIDGE UNIVERSITY PRESS

Variational inference of ice shelf rheology with physics-informed machine learning

Journal:	*Journal of Glaciology*
Manuscript ID	JOG-22-0098
Manuscript Type:	Article
Date Submitted by the Author:	06-Sep-2022
Complete List of Authors:	Riel, Bryan; Zhejiang University, School of Earth Sciences Minchew, Brent; Massachusetts Institute of Technology, Department of Earth, Atmospheric and Planetary Sciences
Keywords:	Glacial rheology, Glacier modelling, Ice dynamics, Ice rheology, Ice shelves
Abstract:	Floating ice shelves that fringe the coast of Antarctica resist the flow of grounded ice into the ocean. One of the key factors governing the amount of flow-resistance provided by an ice shelf is the rigidity of the ice that constitutes it. Ice rigidity is highly heterogeneous and must be calibrated from spatially-continuous surface observations assimilated into an ice flow model. Moreover, realistic uncertainties in calibrated rigidity values are needed to quantify uncertainties in forecasts of future shelf flow. Here, we present a physics-informed machine learning framework for inferring the full probability distribution of rigidity values for a given ice shelf, conditioned on surface velocity and thickness fields derived from remote sensing data. We employ variational inference to jointly

Variational inference of ice shelf rheology with physics-informed machine learning

Bryan RIEL,[1,2] Brent MINCHEW,[2]

[1]*School of Earth Sciences, Zhejiang University, 310027 Hangzhou, China*

[2]*Department of Earth, Atmospheric and Planetary Sciences, Massachusetts Institute of Technology, Cambridge, MA, USA*

Correspondence: Bryan Riel <briel@zju.edu.cn>

ABSTRACT. Floating ice shelves that fringe the coast of Antarctica resist the flow of grounded ice into the ocean. One of the key factors governing the amount of flow-resistance provided by an ice shelf is the rigidity of the ice that constitutes it. Ice rigidity is highly heterogeneous and must be calibrated from spatially-continuous surface observations assimilated into an ice flow model. Moreover, realistic uncertainties in calibrated rigidity values are needed to quantify uncertainties in forecasts of future shelf flow. Here, we present a physics-informed machine learning framework for inferring the full probability distribution of rigidity values for a given ice shelf, conditioned on surface velocity and thickness fields derived from remote sensing data. We employ variational inference to jointly train neural networks and a variational Gaussian Process to reconstruct surface observations and rigidity values and uncertainties. Application of the framework to synthetic and large ice shelves in Antarctica demonstrate that rigidity is well-constrained in areas where deformation of ice is measurable within the noise level of the observations. Further reduction in uncertainties can be achieved by complementing variational inference with conventional inversion methods. Our results demonstrate a path forward for continuous calibration of ice flow parameters from remote sensing observations.

INTRODUCTION

Viscous flow of ice in glaciers and ice sheets is governed by gravitational driving forces and resisting tractions at ice-rock boundaries, as well as internal stresses resulting from stretching and compression. For laterally confined ice shelves that flow within embayments, flow is resisted by shear stresses at the margins where faster-flowing ice is in contact with rock or immobile ice. Basal shear stresses can further resist flow where ice is locally grounded at ice rises or pinning points. The total resistance, or buttressing, provided by ice shelves to upstream grounded ice is a key modulator for potential changes in flow speed of the grounded ice to changes in atmospheric or oceanic conditions. However, accurate quantification of buttressing stresses and modeling of ice shelf flow depends on well-calibrated estimates of ice rheological parameters throughout the modeling domain.

Observations of ice flow, whether in an experimental or natural setting, are the only means by which we can infer mechanical properties such as ice rheology. Specifically, spatially-continuous measurements of flow velocity permit robust estimation of strain rate, which can have considerable spatial variability due to differing flow regimes, rheology, ice geometry, etc. These variations in strain rate are linked to stresses within the ice using an appropriate constitutive law, where the most commonly used relation is Glen's Flow Law:

$$\begin{aligned} \tau_{ij} &= 2\eta\dot{\epsilon}_{ij} \\ &= B\dot{\epsilon}_e^{\frac{1-n}{n}}\dot{\epsilon}_{ij}, \end{aligned} \tag{1}$$

where τ_{ij} is the deviatoric stress tensor, η is the effective dynamic viscosity, B is the ice rigidity, n is the stress exponent, $\dot{\epsilon}_{ij}$ is the strain rate tensor, and $\dot{\epsilon}_e = \sqrt{\dot{\epsilon}_{ij}\dot{\epsilon}_{ij}/2}$ (where we apply the summation convention for repeated indices) is the effective strain rate computed as the square root of the second invariant of the strain rate tensor (Glen, 1958). Note that a prefactor defined as $A = B^{-n}$ is also commonly used in Glen's Flow Law. All of the terms in Equation 1 vary spatially with different intrinsic lengthscales. The stress exponent, n, is set by the dominant mechanisms of creep that drive the deformation of ice and is dependent on the stress regime, grain size, ice temperature, and crystallographic fabric (Goldsby and Kohlstedt, 2001). The prefactor, B, which we refer to as the ice rigidity, shares the same dependencies as the exponent, in addition to interstitial water content, impurities, and damage (Cuffey and Paterson, 2010). Thus, both B and n are lumped parameters in Glen's Flow Law that represent a combination of factors and mechanisms which generally cannot be observed continuously at the scale of ice shelves and ice sheets. Rather, B and n must be inferred from observations of ice surface velocity and elevation for each area of interest.

In order to construct a tractable inverse problem, Glen's Flow Law is first injected into an appropriate dynamical framework (i.e., governing equations for ice flow) in order to obtain a non-linear mapping from parameters (B and n) to observables (ice velocity) over the entire modeling domain. This mapping, or forward problem, can be used in an optimization framework to then estimate the values of the parameters that optimally reconstruct the surface observations (MacAyeal, 1989, 1993). The outcome of the inverse problem, a 2D map of B and n, can then be used in Glen's Flow Law to compute stresses within the ice, which allows for further prognostic simulations to project the evolution of ice flow for a given study area in response to changing climatic conditions. However, for static datasets, i.e. snapshots of velocity and elevation at a given time epoch, B and n cannot be uniquely determined, and independent constraints on one of the parameters is required to reduce the non-uniqueness. In this work, we focus only on inference of a spatially-varying rigidity B, noting that recent work has demonstrated that n may be estimated in Greenland and Antarctica independently under certain flow conditions (e.g., Bons and others, 2018; Millstein and others, 2022), leading to a value of $n \approx 4$ which is consistent with experimental analysis of ice deformation under realistic pressure environments and strain rates (Qi and Goldsby, 2021).

Still, estimation of the optimal rigidity field is equivalent to drawing only a single sample of B from the total statistical *distribution* of fields that could explain the observations nearly equally as well as the optimal one. This distribution is influenced by observational uncertainties as well as modeling uncertainties. For the latter, modeling uncertainties can stem from factors such as model resolution (sensitivity of the forward model to variations in parameter values) and model misspecification where the model fails to capture relevant physics or makes improper assumptions about certain aspects of the physics. Overall, quantification of the distribution of parameter values is of equal importance to estimating the optimal values, and it is ultimately necessary for obtaining a realistic distribution of future ice states conditioned on current-day observations (Aschwanden and others, 2021).

In this work, we aim to develop a framework for estimating the distribution of ice rigidity for large study areas that combines information extracted from relevant surface observations with information obtained from prior theories, experimental/observational studies, etc. While such a framework has a long history in Bayesian inference, our primary consideration in this work is a matter of scalability to large datasets as well as to a large number of effective model parameters. To that end, we build upon recent developments in variational inference and physics-informed machine learning to address the problem of scalability. We use a combination of neural networks for modeling continuous surface observations with variational Gaussian Processes for modeling ice rigidity probability distributions. The mapping between surface observations and rigidity is provided by partial differential equations (PDEs) describing ice flow, which ultimately allow us to include a physics-informed loss function to the training objective for the machine learning models. Both classes of models allow for training with stochastic gradient descent, which is critical for scaling the inference method to large datasets. We target select ice shelves in Antarctica for demonstrating the proposed methods as they provide a number of favorable modeling simplifications while maintaining adequate complexity and large spatial extents suitable for examining the advantages and disadvantages of the proposed methods.

METHODOLOGY

In this section, we will introduce the governing equations for ice flow that link spatial variations in our parameter of interest, ice rigidity, to observations of ice shelf velocity and thickness. We then introduce a physics-informed machine learning framework designed to produce *deterministic* estimates of rigidity consistent with the surface observations. We then recast the framework to produce *probabilistic* estimates of rigidity via Bayesian inference where we utilize variational techniques to perform inference at the scale of large ice shelves, observed with large datasets.

Ice flow force balance forward model

Given a spatial domain with spatial coordinates specified by $\mathbf{x}$, where for two dimensions $\mathbf{x} = [x, y]$, our goal is to estimate the most likely spatial field of ice rigidity, $B = B(\mathbf{x})$, conditional on observations of the flow of ice shelves and their geometry. To that end, we utilize a force balance method to estimate B that computes resistive stresses that optimally balance gravitational driving stresses. Within ice shelves, resistive (vertical) shear stresses at the base are negligible due to contact with seawater, and ice is a thin film such that thicknesses are small relative to the aerial extent. Thus, we are justified in employing the widely-used shallow shelf approximation (SSA), which assumes negligible vertical shearing in a thin film and vertically integrates viscosity and stresses in the ice column to obtain a simplified 2D framework for the governing equations of flow in ice shelves:

$$\frac{\partial}{\partial x}\left(2\eta h\left(2\frac{\partial u}{\partial x}+\frac{\partial v}{\partial y}\right)\right)+\frac{\partial}{\partial y}\left(\eta h\left(\frac{\partial u}{\partial y}+\frac{\partial v}{\partial x}\right)\right)-\tau_{bx}=\rho_i g h\frac{\partial s}{\partial x}, \tag{2}$$

$$\frac{\partial}{\partial y}\left(2\eta h\left(2\frac{\partial v}{\partial y}+\frac{\partial u}{\partial x}\right)\right)+\frac{\partial}{\partial x}\left(\eta h\left(\frac{\partial u}{\partial y}+\frac{\partial v}{\partial x}\right)\right)-\tau_{by}=\rho_i g h\frac{\partial s}{\partial y}, \tag{3}$$

where u and v are the horizontal velocity components of the velocity vector, $\boldsymbol{u}$, along the x- and y-directions, respectively, and taken to be constant with depth; h is the ice thickness; s is the ice surface elevation; $\eta = \frac{1}{2}B\dot{\epsilon}_e^{\frac{1-n}{n}}$ is the effective dynamic viscosity of ice; ρ_i is the mass density of ice; and g is the gravitational acceleration. In the above formulation, we also include terms for the basal drag in both directions, τ_{bx} and τ_{by}, in order to parameterize force balance *residuals*. Since drag at the base of ice shelves is assumed to be negligible, we seek to construct the field $B(\mathbf{x})$ that minimizes τ_{bx} and τ_{by}. This strategy of using the SSA-based force balance as our forward model has the key advantage of allowing for computation of τ_{bx} and τ_{by} at each spatial point independently, requiring only observations of velocity gradients and ice thickness values and gradients. The forward model can therefore be evaluated over a large spatial domain in parallel. However, gradients of velocity and thickness still implicitly have spatial dependencies, which will correspondingly influence the inference of $B(\mathbf{x})$. As described below, the former is addressed using neural networks and the latter is addressed via the construction of an appropriate prior distribution for B.

Physics-informed neural networks for observations and flow law prefactor

Observations of horizontal ice velocity over ice sheet margins have been widely available for the past decade thanks to the prevalence of remote sensing platforms and efficient data processing methodologies (Joughin and others, 2010; Mouginot and others, 2017; Gardner and others, 2019). At the same time, improved integration of ice penetrating radar and surface velocities using mass conservation techniques have allowed for more accurate and higher resolution maps of ice thickness and bathymetry (Morlighem and others, 2017). Specifically over ice shelves, it is common practice to convert observations of surface elevation, which are well constrained, to ice thickness by assuming hydrostatic equilibrium and applying corrections for firn layers derived from in situ thickness data (Morlighem and others, 2020). Thus, when velocity and thickness observations are spatially continuous over an ice shelf, we can estimate spatial gradients and compute the SSA force balance directly. However, observation noise and data gaps generally degrade estimates of observation gradients, which can then result in non-physical estimates of SSA forces which require an additional gradient operation. We therefore require a rigorous method to approximate the continuous functions that generate large datasets of surface velocity and ice thickness in a manner that optimally balances reconstruction accuracy of the observed data while resulting in reasonable estimates of SSA forces. Such methods can be broadly classified as function approximators, examples of which include Gaussian processes (Rasmussen, 2003), polynomial chaos expansion (Ernst and others, 2012), and neural networks (Cybenko, 1989; Bölcskei and others, 2019). For our purposes, we seek function approximators that allow for optimization objectives that factorize across individual data examples, which is a necessary condition for dealing with very large datasets. To that end, we first use a dense, feedforward neural network, f_{ψ}, to represent the surface observations on a point-by-point basis:

$$\hat{\mathbf{d}}_i = f_{\psi}\left(\mathbf{x}_i\right), \tag{4}$$

where $\hat{\mathbf{d}}_i = [\hat{u}_i, \hat{v}_i, \hat{h}_i]$ is the vector of neural network predictions at the i-th coordinate $\mathbf{x}_i$, and $\boldsymbol{\psi}$ represents the total set of weights and biases of the hidden layers. One can then estimate the optimal $\boldsymbol{\psi}$ through an optimization procedure (i.e., neural network training) that adjusts the values of $\boldsymbol{\psi}$ in order to minimize some cost function, e.g. mean square error between the observed and predicted velocities and thicknesses:

$$J_{\mathrm{mse}}(\boldsymbol{\psi}) = \frac{1}{M}\sum_{i=1}^{M}(\hat{\mathbf{d}}_i - \mathbf{d}_i)^T(\hat{\mathbf{d}}_i - \mathbf{d}_i), \tag{5}$$

where M is the number of data points used for training and $\mathbf{d}_i = [u_i, v_i, h_i]$ is the vector of observations at the i-th data point. To avoid overfitting of the observation noise, some form of regularization is required, either directly on $\boldsymbol{\psi}$ or by introducing another cost function that would encourage spatially-smoother predictions of $\hat{\mathbf{d}}$ (Riel and others, 2021). Here, we follow the latter strategy by constructing a cost function that combines the standard reconstruction mean square error with the SSA equations from the previous section and a function quantifying prediction smoothness in space.

We now introduce a second function approximator, g_{φ}, tasked with predicting the flow law prefactor at a given location:

$$\hat{B}_i = g_{\varphi}\left(\mathbf{x}_i\right), \tag{6}$$

where $\boldsymbol{\varphi}$ corresponds to the parameters of g_{φ}. At this point in the discussion, g_{φ} can be any appropriate function approximator, provided that its optimization objective can be factorized across data examples and that gradients of the outputs of g_{φ} with respect to its inputs, $\mathbf{x}_i$, can be efficiently computed. With both f_{ψ} and g_{φ}, we can thus compute spatial gradients at an arbitrary spatial coordinate, allowing us to then evaluate the residual terms τ_{bx} and τ_{by} in the SSA equations. Since these residuals are nominally zero for ice shelves, we can construct a *physics-based* cost function:

$$J_{\text{ph}}(\boldsymbol{\psi}, \boldsymbol{\varphi}) = \frac{1}{P} \sum_{i=1}^{P} (\tau_{bxi}^2 + \tau_{byi}^2), \tag{7}$$

where P is now the number of spatial points used for evaluating J_{ph}. While the above cost function provides a means to optimize $\boldsymbol{\varphi}$, it still does not provide a way to mitigate observation noise since both f_{ψ} and g_{φ} will generate predictions with potentially high variance in order to overfit the observations. Therefore, we introduce a third cost function that measures the spatial roughness of the $\hat{B}$ field. Penalizing parameter roughness has a long history in geophysical inversion methods, including parameter estimation for discretized numerical ice flow models (MacAyeal, 1993; Morlighem and others, 2010; Habermann and others, 2013; Gillet-Chaulet and others, 2016). Any number of roughness metrics can be used, and in this work, we opt for a Gaussian-weighted spatial correlation measure (described in detail in the next section). For now, we denote the roughness cost function as $J_R(\boldsymbol{\varphi})$, and we can write the final combined loss function for jointly optimizing $\boldsymbol{\psi}$ and $\boldsymbol{\varphi}$:

$$J(\boldsymbol{\psi}, \boldsymbol{\varphi}) = \lambda_1 J_{\text{mse}}(\boldsymbol{\psi}) + \lambda_2 J_{\text{ph}}(\boldsymbol{\psi}, \boldsymbol{\varphi}) + \lambda_3 J_R(\boldsymbol{\varphi}),$$

where the λ_i scalar parameters correspond to penalty parameters that adjust the relative contributions of the different different loss functions in J. While values for λ_i can be chosen using standard model selection techniques like cross validation, we opt to recast the entire optimization problem as a probabilistic problem such that the λ_i values correspond to inverses of concrete values like observation variance, prior variance, etc. The probabilistic problem can then be solved efficiently using variational inference, as described in Section .

Model dimensionality

Unlike standard numerical modeling approaches where the model domain is discretized (e.g., using finite elements) we instead treat each variable as a continuous surface represented by a specific neural network. Therefore, statements of model dimensionality in this work are not exactly analogous to the usual specification of dimensionality dictated by the number of finite elements. In our case, a "high-dimensional" model is one where we would expect the modeling domain to span a wide area with substantial variation of the parameter field within the domain. In such a case, one would typically require a large number of finite elements in order to accurately reconstruct the parameter field. While an equivalent neural network may actually have a higher number of total parameters (weights and biases of the hidden layers) than a finite element parameterization, optimization of these parameters tend to use first-order gradient-based methods, which are generally more computationally efficient than second-order methods applied to optimization of finite element-based inversion problems.

Probabilistic formulation of inference problem

In the previously discussed optimization framework, a deterministic cost function is minimized in order to train a pair of function approximators to reconstruct observations of ice surface velocity and thickness and to predict a spatially continuous field for the ice rigidity, $B(\mathbf{x})$. However, one of the main goals of this work is to rigorously quantify the uncertainties associated with B, conditioned on the observations and the 2D SSA framework. Equivalently, we seek to draw realistic random samples of B that are consistent with the observations, maintain sufficient spatial resolution, and exhibit spatial correlations that are physically consistent with known physics. To that end, we utilize Bayes' Theorem to construct the posterior probability distribution for B given a set of observations. Since our forward problem is reduced to computation of the the force balance of the 2D SSA equations, the forward model predictions and corresponding "observations" are just the residual drag vector, $\boldsymbol{\tau}_b = [\tau_{bx}, \tau_{by}]$, which is nominally zero. The continuous posterior distribution for B is then

$$p(B|\boldsymbol{\tau}_b) \propto p(\boldsymbol{\tau}_b|B)p(B), \tag{8}$$

where the first distribution on the right-hand side is the data likelihood, which encodes the probability of having "observed" $\boldsymbol{\tau}_b$ for a given B within the SSA equations, and the second distribution is the prior, which encodes our prior knowledge on B values without having seen any observations.

Data likelihood

The vector $\boldsymbol{\tau}_b$, which is nominally zero for ice shelves, is a pseudo-observation that incorporates information from the actual surface observations, $\mathbf{d}$, as well as the current value of B, i.e. $\boldsymbol{\tau}_b = \boldsymbol{\tau}_b(B, \mathbf{d})$. As such, uncertainties in both $\mathbf{d}$ and B will propagate to $\boldsymbol{\tau}_b$, e.g.,

$$\sigma^2_{\boldsymbol{\tau}_b} = \left(\frac{\partial \boldsymbol{\tau}_b}{\partial B}\right)^2 \sigma^2_B + \left(\frac{\partial \boldsymbol{\tau}_b}{\partial \mathbf{d}}\right)^2 \sigma^2_{\mathbf{d}}.$$

Prescribing a proper value of $\sigma^2_{\boldsymbol{\tau}_b}$ for the likelihood distribution involves a careful consideration of the observation uncertainties and the expected uncertainties in B. Additionally, it is possible to encounter situations where the SSA (with zero basal drag) will perform poorly, such as pinning points where ice shelves become locally grounded over bathymetric highs. These *epistemic* uncertainties will also implicitly affect the underlying distribution of $\sigma^2_{\boldsymbol{\tau}_b}$. In practice, we estimate $\sigma^2_{\boldsymbol{\tau}_b}$ using the above propagation of uncertainties for known observational variances, $\sigma^2_{\mathbf{d}}$, and a conservative scalar estimate for σ^2_B. We then use an independent normal distribution for the data likelihood (spatially independent and independent for each component of $\boldsymbol{\tau}_b$):

$$p(\tau_{bi}) = \mathcal{N}(0, \sigma^2_{\tau_{bi}}). \tag{9}$$

The likelihood formulation can be improved by incorporation of spatially-correlated uncertainties, explicit handling of epistemic uncertainties (see Section), and by using a non-Gaussian probability distribution, where choice of the latter can be guided by Monte Carlo sampling. We leave these improvements for future exploration.

Prior distribution

In order to encourage spatial smoothness in B, we construct a multivariate normal prior distribution that encourages spatial coherence between predictions of B at different coordinates, e.g., $\mathbf{x}_1 = [x_1, y_1]$ and $\mathbf{x}_2 = [x_2, y_2]$:

$$\begin{aligned} p([B(\mathbf{x}_1), B(\mathbf{x}_2)]) &\sim \mathcal{N}(\mathbf{B_0}, \boldsymbol{\Sigma}_B) \\ \boldsymbol{\Sigma}_B &= \sigma^2_B \exp\left(\frac{\delta\mathbf{x}^T \delta\mathbf{x}}{2L^2}\right), \end{aligned} \tag{10}$$

where $\mathbf{B_0} = [B_0(\mathbf{x}_1), B_0(\mathbf{x}_2)]$ is the prior mean vector, σ^2_B is the prior variance, $\delta\mathbf{x} = \mathbf{x}_1 - \mathbf{x}_2$, and L is a prescribed correlation lengthscale. The field $B_0(\mathbf{x})$ may be assigned using tabulated values of ice rheology dependence on temperature (e.g., Cuffey and Paterson, 2010) or from previous studies. Effectively, this prior is equivalent to smoothing of the predictions of B using a Gaussian kernel while encouraging values to not vary too far from B_0. This approach can be especially useful when B_0 is derived from *in situ* estimates in order to calibrate the remote sensing-derived estimates. Strictly speaking, B has a positivity constraint, which would require the use of a truncated distribution for the prior. A common approach in this case is to define a normalized ice rigidity $\theta = \theta(\mathbf{x})$ such that $B = B_0 e^{\theta}$. In this case, the prior distribution would be transformed to:

$$
\begin{aligned}
p([\theta(\mathbf{x}_1), \theta(\mathbf{x}_2)]) &\sim \mathcal{N}(\mathbf{0}, \mathbf{\Sigma}_\theta) \\
\mathbf{\Sigma}_\theta &= \sigma_\theta^2 \exp\left(\frac{\delta\mathbf{x}^T \delta\mathbf{x}}{2L^2}\right),
\end{aligned} \tag{11}
$$

where σ_θ^2 is now the prior variance for θ. In practice, we use the prior $p(\theta)$ and posterior $p(\theta|\mathbf{d})$ to formulate the probabilistic problem, and in later discussions analyzing posterior predictions, we will transform samples of θ to B.

For Bayesian inference in general, selection of the prior $p(\theta)$ can have a large influence on the estimated posterior $p(\theta|\mathbf{d})$, depending on data uncertainties, data location, model resolution, etc. For our purposes, since we assume a multivariate normal distribution for $p(\theta)$, the two main tuning parameters are the prior mean and the prior covariance structure controlled by the covariance lengthscale, L, and the variance, σ_0^2. For the prior mean, since our control variable is θ, prescribing B_0 is the primary approach by which we can control the influence of the mean on posterior inference. In this work, we investigate two different strategies: i) assume that B_0 is uniform (uniform ice temperature); or ii) estimating B_0 independently through an inversion using traditional control methods. For the second strategy, recall that traditional control methods generally use an optimization objective based on the misfit between observed and predicted ice velocities, which is different from the force balance optimization objective used here. Therefore, the velocity misfit-based objective will implicitly have different spatially-varying sensitives to the parameter field than the force balance objective, which provides an opportunity to combine the two objectives in a complementary manner. For the two different strategies for selecting the prior mean, we also correspondingly adjust the prior variance. When the prior mean is relative to a uniform B_0, we set $\sigma_\theta^2 = 1$ to allow for a relatively large variation in θ over the ice shelf. When the prior mean is relative to a B_0 obtained from a control method inversion, we reduce σ_θ^2 to 0.2, which encodes our belief that the values of B from the inversion are relatively well-constrained, and θ thus represents smaller deviations of B dictated by the force balance optimization objective.

Posterior inference using variational Gaussian Processes

Due to non-linearities in the forward problem (SSA force balance) and a potentially non-Gaussian data likelihood, the posterior for θ must be approximated, either by drawing random samples from $p(\theta|\boldsymbol{\tau}_b)$ or by constructing a suitable approximating distribution. The former strategy is based on the general class of Markov Chain Monte Carlo (MCMC) approaches and tends to be suitable for a low or moderate number of model dimensions. As we stated earlier, in our neural network formulation, the concept of model dimensionality is not directly applicable when considering the feasibility of MCMC approaches. Instead, we seek to quantify the distribution of functions that best approximate a certain variable field, which is similar to the aim of Gaussian Processes (Rasmussen, 2003). To that end, we employ a variational inference framework wherein we aim to construct an approximating distribution for θ, $q(\theta)$, that is minimally divergent from the true posterior $p(\theta|\boldsymbol{\tau}_b)$.

Specifically, we train a variational Gaussian Process (VGP) to predict $q(\theta)$, which utilizes the concept of sparse *inducing index points* for approximating large datasets (Titsias, 2009). For n data points indexed by location variables $\mathbf{x}$, inference with Gaussian processes have a computational complexity of $\mathcal{O}(n^3)$ and memory requirements of $\mathcal{O}(n^2)$, both of which can be prohibitive for datasets larger than a few thousand examples. To overcome this limitation, rather than performing inference on the entire dataset, inference can be performed on inducing points such that function values at non-inducing points (i.e., data points) are mutually independent and conditional on function values at the inducing points. For m inducing points indexed by location variables $\mathbf{z}$ (assuming $\mathbf{z}$ independent from $\mathbf{x}$ and $m \ll n$), the computational complexity is reduced to $\mathcal{O}(nm^2)$ while the memory requirements are reduced to $\mathcal{O}(m^2)$. With this approach, we can then create an approximating variational distribution at the inducing index points, such that the inducing point locations, mean values, and covariance matrix comprise the tunable parameters of an approximating multivariate normal distribution. Prediction of θ values at arbitrary coordinates is facilitated by standard evaluation of a Gaussian Process kernel function where the inducing index points form one component of the coordinate pair (Hensman and others, 2013). Therefore, the hyperparameters of the kernel function are combined with the tunable parameters of the variational distribution to form the set of trainable variational parameters $\boldsymbol{\varphi}$ for $g_{\boldsymbol{\varphi}}$.

Optimization of the variational parameters requires an objective function that quantifies some measure of similarity between the variational and target posterior distributions. A commonly used probabilistic metric is the Kullback-Leibler (KL) divergence, which when evaluated at the inducing and data point locations takes the following form:

$$\mathcal{KL}\left[q(\theta_{\mathbf{z}}, \theta_{\mathbf{x}})||p(\theta_{\mathbf{z}}, \theta_{\mathbf{x}}|\boldsymbol{\tau}_b)\right] = \int q(\theta_{\mathbf{z}}, \theta_{\mathbf{x}}) \log \frac{q(\theta_{\mathbf{z}}, \theta_{\mathbf{x}})}{p(\theta_{\mathbf{z}}, \theta_{\mathbf{x}}|\boldsymbol{\tau}_b)} d\theta_{\mathbf{z}} d\theta_{\mathbf{x}}. \tag{12}$$

The KL-divergence is a generalization of distance applied to probability distributions. By minimizing the KL-divergence, we are tuning the variational distribution to be close to the target posterior distribution from an informational perspective. However, evaluation of $p(\theta_{\mathbf{z}}, \theta_{\mathbf{x}}|\boldsymbol{\tau}_b)$ is typically intractable due to an integral in the evidence (which needs to be evaluated for all possible values of B). In this case, it can be shown (e.g., Titsias, 2009; Matthews and others, 2016; Blei and others, 2017) that minimization of the KL-divergence (denoted by $\mathcal{KL}\left[q(\theta)||p(\theta)\right]$ for brevity) can be replaced by maximization of a variational lower bound, often referred to as the Evidence Lower Bound (ELBO):

$$\begin{aligned}
\text{ELBO} &= E_{\theta \sim q(\theta_{\mathbf{x}})}\left[\log \mathcal{N}(\tau_b|\theta, \sigma_{\tau_b})\right] - \mathcal{KL}\left[q(\theta_{\mathbf{z}})||p(\theta_{\mathbf{z}})\right] \\
&= \frac{1}{P}\sum_{i=1}^{P}\left[\log \mathcal{N}(\tau_{b_i}|\theta_i, \sigma_{\tau_{b_i}})\right] - \mathcal{KL}\left[q(\theta_{\mathbf{z}})||p(\theta_{\mathbf{z}})\right].
\end{aligned} \tag{13}$$

The first term on the right side of the above equation is a Monte Carlo approximation of the data likelihood as before evaluated at P data points $\mathbf{x}$, using $\theta(\mathbf{x})$ sampled from the variational distribution q. Since we assume independence in the likelihood between different locations $\mathbf{x}$, the expectation factorizes into a sum of one-dimensional log-likelihoods, meaning it can be evaluated on a per-example basis where each example is evaluated with an independent θ_i sampled from the variational distribution. In practice, the size of P is specified by the batch size used during training, where smaller batches allow for more efficient evaluation of $q(\theta)$ but higher variance in the likelihood estimation. In order to reduce the variance of the likelihood during training and reduce the dependence on the batch size, we follow the approach of Dillon and others (2017) and replace the summation with a Gauss-Hermite quadrature, which is exact for Gaussian likelihoods. It is important to reiterate that for the log-likelihood, the neural network f_ψ is still evaluated in order to compute τ_b, so its parameters will influence the value of the ELBO and thus are still a subset of the tunable parameters. The second term in Equation 13 is the KL-divergence between the variational distribution and the prior distribution evaluated at the inducing index points. Note that the multivariate normal prior introduced in Equation 10 is mathematically equivalent to using a radial basis function (RBF) kernel, which we use as the kernel for the VGP. Overall, Equation 13 can be interpreted as an optimization objective that encourages the variational distribution to predict B that minimizes the basal drag while also maintaining consistency with the prior distribution.

Joint Training Objective

The final component of the probabilistic formulation is specification of the cost function for reconstructing the ice surface velocity and thickness. Here, we replace the mean-square error cost function in Equation 5 with independent normal distributions:

$$p(u_i) \sim \mathcal{N}(\hat{u}_i, \sigma_{ui}^2),$$
$$p(v_i) \sim \mathcal{N}(\hat{v}_i, \sigma_{vi}^2),$$
$$p(h_i) \sim \mathcal{N}(\hat{h}_i, \sigma_{hi}^2),$$

where i denotes the i-th observation, the hat variables are those predicted by $f_{\boldsymbol{\theta}}$, and the different σ^2 variables correspond to the variances of each observation component. The observation variances may be prescribed or learned, and in this work, we fix the variances to scaled values of formal observation uncertainties (using a scale factor of 10-30). The total likelihood for the independent distributions is then $p(u_i, v_i, h_i) = p(u_i)p(v_i)p(h_i)$. Finally, the total probabilistic loss function for joint training of f_{ψ} and g_{φ} is:

$$J(\boldsymbol{\psi}, \boldsymbol{\varphi}) = J_{data}(\boldsymbol{\psi}) + \mathrm{ELBO}(\boldsymbol{\psi}, \boldsymbol{\varphi}), \tag{14}$$

where

$$J_{data}(\boldsymbol{\psi}) = \frac{1}{M}\sum_{i=1}^{M}\left[\log p(u_i) + \log p(v_i) + \log p(h_i)\right],$$

for M observations. A summary of the neural network and variational inference training framework is described in Figure 1.

Generating shelf-wide samples of the ice rigidity

While the VGP utilizes inducing index points to allow for per-batch prediction of θ and the corresponding posterior covariance matrices, we still require an algorithm for generating a random sample of θ with a given spatial resolution over the entire modeling domain. The usual approach of assembling global mean and covariance matrices for the entire domain would be memory-intensive for uniform grids with sizes exceeding

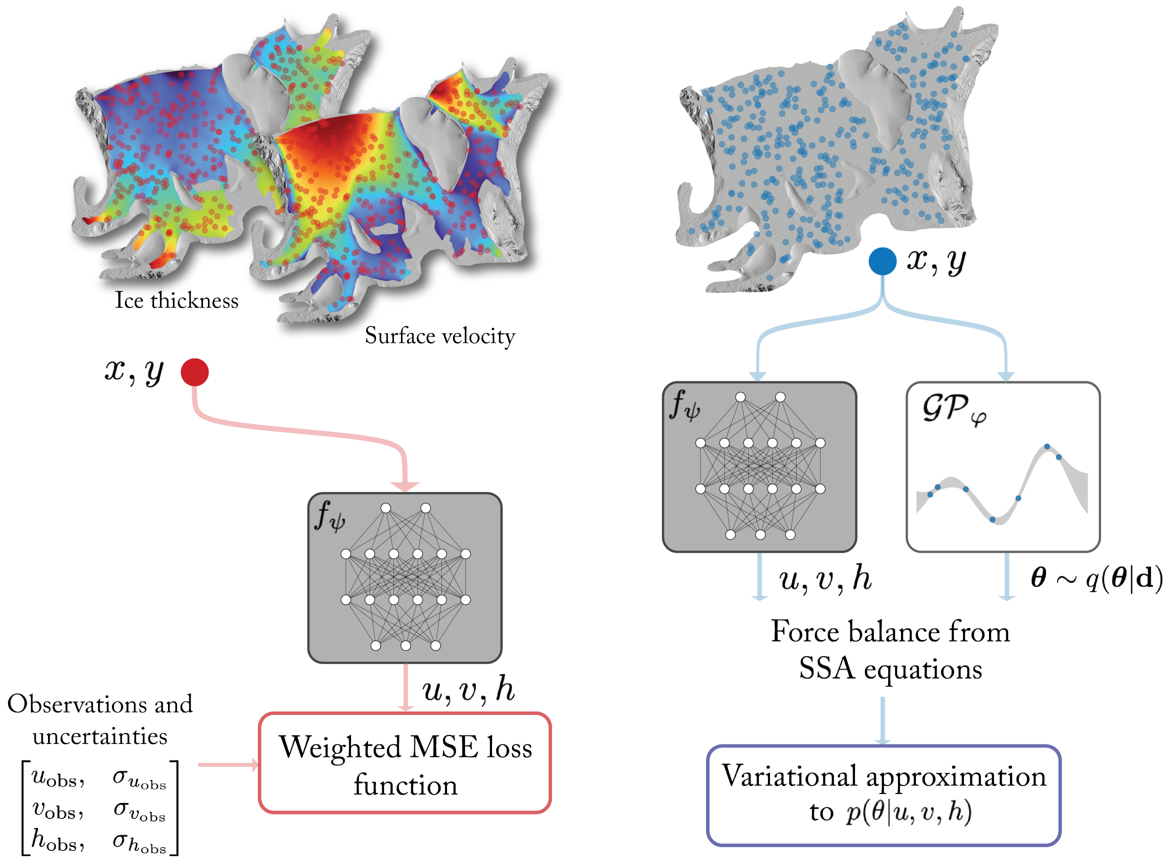

Fig. 1. Illustration of physics-informed variational inference framework. The two main components of the framework are the neural network f_ψ tasked with reconstructing surface observations (grey box) and the variational Gaussian process $\mathcal{GP}_\varphi$ tasked with modeling the distribution $q(\theta|\mathbf{d})$ (white box), which is a variational approximation to the posterior distribution of the normalized ice rigidity parameter θ. The training loss function is the sum of: 1) a weighted mean square error (MSE) loss between the predicted and observed observations; and 2) a variational lower bound to the KL-divergence between $q(\theta|\mathbf{d})$ and the true posterior distribution $p(\theta|u, v, h)$. For the MSE loss, training data and corresponding uncertainties and spatial coordinates are sampled from remote sensing observations (red dots). For the variational loss, an independent set of spatial coordinates (blue dots) are sampled from the model domain, which are input to f_ψ and $\mathcal{GP}_\varphi$ in order to evaluate the SSA force balance at those coordinates.

tens of thousands of grid points. We therefore utilize an MCMC-based approach where a random sample of θ is generated at some coordinate within the ice shelf and used as a seed to grow a full chain over the entire shelf. In this work, we apply Gibbs sampling on a block-by-block basis where a block is defined as a small subset of the uniform grid. For each block, the mean $\boldsymbol{\mu}_\theta$ and covariance matrix $\mathbf{C}$ are computed using the trained VGP. A random chain is then seeded by a random sample from a given block (using a multivariate normal distribution) and propagated through the entire ice shelf by computing Schur complements on a block-by-block basis. For a given block, the Schur complement computes the mean and covariance matrix used for generating a sample of θ, conditional on the statistics of the previous block. As an example, assume that the first two blocks are combined in the following partition:

$$\boldsymbol{\theta} = \begin{bmatrix} \boldsymbol{\theta}_1 \\ \boldsymbol{\theta}_2 \end{bmatrix}, \quad \boldsymbol{\mu} = \begin{bmatrix} \boldsymbol{\mu}_1 \\ \boldsymbol{\mu}_2 \end{bmatrix}, \quad \mathbf{C} = \begin{bmatrix} \mathbf{C}_{11} & \mathbf{C}_{12} \\ \mathbf{C}_{21} & \mathbf{C}_{22} \end{bmatrix} \tag{15}$$

Then, initializing a Gibbs chain uses the following identities:

$$\boldsymbol{\theta}_1 \sim \mathcal{N}(\boldsymbol{\mu}_1, \mathbf{C}_{11}), \tag{16a}$$

$$\boldsymbol{\theta}_2 \sim \mathcal{N}\left(\boldsymbol{\mu}_2 + \mathbf{C}_{21}\mathbf{C}_{11}^{-1}(\boldsymbol{\theta}_1 - \boldsymbol{\mu}_1), \mathbf{C}_{22} - \mathbf{C}_{21}\mathbf{C}_{11}^{-1}\mathbf{C}_{12}\right). \tag{16b}$$

We then set $\boldsymbol{\mu}_1 \leftarrow \boldsymbol{\mu}_2$, $\boldsymbol{\theta}_1 \leftarrow \boldsymbol{\theta}_2$, and $\mathbf{C}_{11} \leftarrow \mathbf{C}_{22}$ and apply Equation 16b for the next block to proceed over the entire modeling domain. In our experiments, we found that if the block size was chosen to be too small, the variance of the final sample was artificially large, likely due to excessive truncation of the covariance matrix (depending on the resolution of the uniform grid). Here, we found a block size of 1000 works well for grids with cell sizes equal to roughly half or a quarter of the prior covariance lengthscale.

Related work

Bayesian inference has long been applied to geophysical inverse problems, and as computational resources and inference algorithms improve, the complexity and size of the physical models investigated has increased. Within glaciological inverse problems, Bayesian formulations of the posterior distributions have been used as cost functions for obtaining point estimates of basal topography and friction for grounded ice streams (Pralong and Gudmundsson, 2011). For fully Bayesian inference, Petra and others (2014) developed an MCMC method for estimating the posterior distribution for ice sheet models with a large number of parameters, utilizing low-rank approximations of data likelihood Hessian matrices in order to reduce computational complexity while improving sample efficiency. Similarly, Gopalan and others (2021) used a Gibbs sampler in order to sample for ice stream model parameters for a simpler model applicable to slower-flowing ice. While MCMC methods generally serve as "gold standards" for Bayesian inference, they do not scale well to large problem sizes. MCMC methods that invoke simpler proposal distributions usually require many more samples in order to sufficiently sample the posterior, whereas methods that can utilize the problem structure to improve sample efficiency require more computational resources (Petra and others, 2014).

Methods that approximate the posterior distribution, rather than sample from it, provide appealing alternatives to MCMC. Both Isaac and others (2015) and Babaniyi and others (2021) utilize a Gaussian approximation of the posterior centered on the *maximum a posteriori* (MAP) point (i.e., a Laplace approximation) in order to infer basal drag parameters for ice sheets. While Laplace approximations subvert the need for generating posterior samples (and the forward model evaluations associated with each sample), they can lead to posterior approximations that fail to capture much of the probability mass when the posterior is sufficiently non-Gaussian or multi-modal (Penny and others, 2007). In contrast, variational methods that utilize the KL-divergence as an optimization criterion (as done here) tend to favor approximating distributions that match the moments of the target distribution (e.g., mean and variance), which tends to capture more probability mass. Sufficient capturing of probability mass can be especially important for posterior predictive modeling where non-linearities can lead to a large spread of predictions (e.g., Section).

To that end, Brinkerhoff (2022) introduced a variational inference method to jointly infer basal drag and ice rheology at a catchment-scale for glaciers. Importantly, the KL-divergence was used to estimate an optimal approximating distribution that also uses a Gaussian process prior, similar to the approximating distributions used in our work. A finite number of eigenvectors of the prior covariance are used to construct a linear model that permits inference at a lower dimension. The construction of the eigenvectors utilizes a coarse spatial grid that is analogous to the inducing points used in this work. Thus, the method of Brinkerhoff (2022) shares many of the same features proposed here, with two main differences. Firstly, we use the momentum balance based on the SSA as our forward model in order to compute τ_b, whereas all the previous approaches discussed here use predicted velocities which require solving a large-scale PDE problem. The former is separable and can be computed in parallel, which is crucial for using batch-based stochastic gradient descent for large datasets. However, this choice of forward model will lead to different sensitivities to the ice rheology parameters (more discussion in Section). The second difference is related to the first in that we utilize neural networks to model the ice surface variables, which is also amenable to stochastic gradient descent. The use of neural networks with automatic differentiation allows for a mesh-free evaluation of higher-order spatial gradients needed for the SSA momentum balance.

APPLICATION TO SIMULATED ICE SHELVES

We now apply the physics-informed variational framework to simulated ice shelves in order to evaluate the recovery of ice rigidity under varying degrees of model complexity and uncertainty and data noise. Furthermore, the simulated ice shelves allow us to isolate which mechanical factors control the inferred rigidity uncertainties, which will aid in building intuition for application of the framework to natural settings.

1D Ice Shelf

We first simulate a laterally-confined ice shelf using 1D SSA equations where lateral drag is parameterized assuming a rectangular bed with width w in the across-flow direction (Nick and others, 2010). The momentum equation in the along-flow direction reduces to:

$$\frac{\partial}{\partial x}\left(4\eta h\frac{\partial u}{\partial x}\right) - \frac{2Bh}{w}\left(\frac{5u}{w}\right)^{1/n} = \rho_i g h\frac{\partial s}{\partial x}. \tag{17}$$

We simulate an ice shelf with a width of 30 km and a length of 100 km, which is comparable to ice shelves of several ice streams in West Antarctica, such as Rutford Ice Stream. We prescribe a spatially-varying B profile that is periodic in the along-flow direction while setting the flow law exponent to be uniform at $n = 3$. After simulating the shelf for 400 years to an approximate steady-state, we extract 200 random velocity and thickness values over the model domain to use as training data. We add spatially-correlated noise by convolving a 1D field of independent Gaussian noise with a Gaussian kernel with a lengthscale of 5 km. We train a feedforward neural network with four hidden layers of 50 nodes each in order to reconstruct the velocity and thickness and a VGP with 15 inducing index points in order to predict the normalized prefactor variable θ. We use an *a priori* value of the prefactor $B_0 = 400$ yr$^{1/3}$ kPa. For the prior distribution for θ, we describe a prior standard deviation of $\sigma_\theta = 1$ and a correlation lengthscale

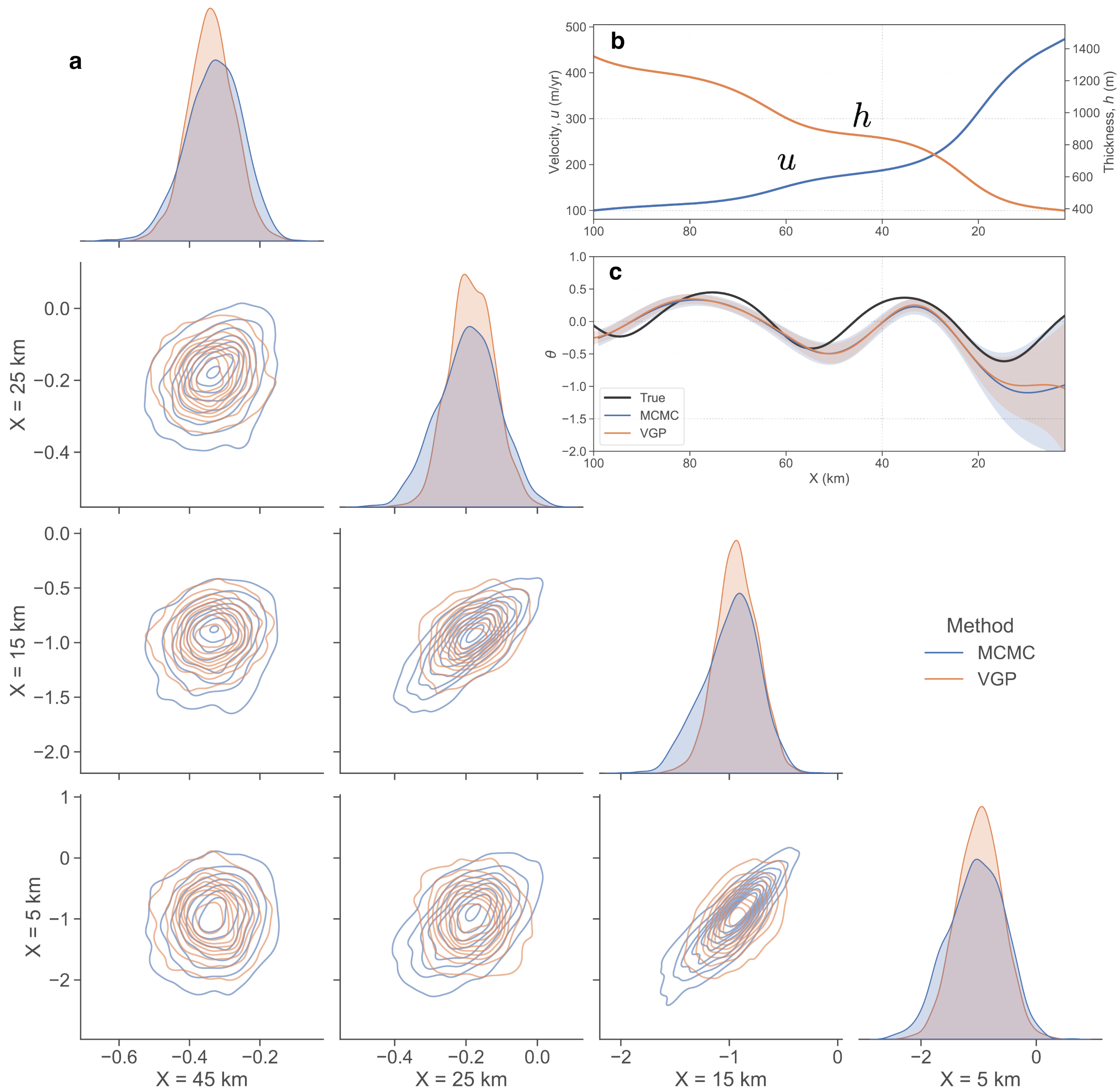

Fig. 2. Posterior inference of ice rigidity for simulated 1D ice shelf. a) Posterior marginal distributions for θ at different locations along the ice shelf. The grounding line is at $X = 0$ km and the ice front is at $X = 100$ km. Diagonal plots show the 1D marginals computed from posterior samples generated with MCMC (blue) and the variational Gaussian process (VGP; orange). Off-diagonal plots show 2D covariance plots for the same sample set. All marginals have been smoothed using a Gaussian kernel density estimator. b) Velocity (blue) and ice thickness (orange) of ice shelf used for posterior inference. c) Comparison of the true $\theta(X)$ against the mean $\theta(X)$ computed from the MCMC samples (blue) and the VGP (orange). The shaded regions correspond to 2σ posterior uncertainties. Overall, the posterior distributions for MCMC and VGP are very similar. The largest deviations occur near the ice front where the marginals exhibit stronger non-Gaussian behavior, which cannot be modeled by the VGP.

of 15 km. For the data likelihood parameterizing the residual basal drag, we use an independent normal distribution with a mean of zero and a standard deviation of $\sigma_{\tau_b} = 2.0$.

As is commonly done in studies investigating variational inference techniques to approximate a target posterior distribution, we compare the estimated variational distribution with direct samples from the posterior using MCMC. Here, we utilize a No U-Turn Sampler scheme implemented in the `NumPyro` Python package (Phan and others, 2019), which uses automatic differentiation to efficiently generate sample trajectories for moderately high numbers of model parameters.

We find that both MCMC and variational inference recover a posterior mean profile for θ that is close to the true values for areas greater than 20 km upstream from the ice front (Figure 2). Close to the ice front, both methods predict uncertainties that are substantially larger due to thinner ice, which reduces the sensitivity of the longitudinal and lateral membrane stresses (left-hand terms in Equation 17) to rigidity variations. Pair plots of marginal distributions of θ at different locations along the ice shelf show that the variational approach is able to recover strong covariances between θ samples for locations that are relatively close to each other while ensuring samples are uncorrelated for larger pair-wise distances. In general, the strength of the posterior covariance will be modulated by the physical model as well as the prior correlation lengthscale. Closer to the ice front, the marginal distributions derived from MCMC indicate a slight deviation from Gaussian behavior, which is again likely due to the lower ice thicknesses limiting ice stress sensitivity to rigidity variations. Since the variational distribution is constrained to be a multivariate normal, it is unable to recover the non-Gaussian behavior in the marginals in these areas. However, as documented in previous studies (e.g., Huszár, 2015; Albergo and others, 2021), training the variational distribution with a reverse-KL divergence loss encourages mode-seeking behavior (but does not enforce it like the Laplace approximation), i.e. the distribution will be centered closer to regions with the highest posterior probabilities. For applications where it is desirable to fully explore parameter regions with non-zero posterior probabilities, one could simply increase relevant variances (σ_θ, σ_{τ_b}) or use a more flexible variational approximation not restricted to multivariate normals (Rezende and Mohamed, 2015).

2D Ice Shelf

We now simulate a 2D ice shelf using the `icepack` ice flow modeling software (Shapero and others, 2021). Similar to the synthetic ice shelf presented in Shapero and others (2021), we prescribe a semi-circular shelf geometry with four inlet glaciers of varying widths (Figure 3). Additionally, we prescribe a bed topography

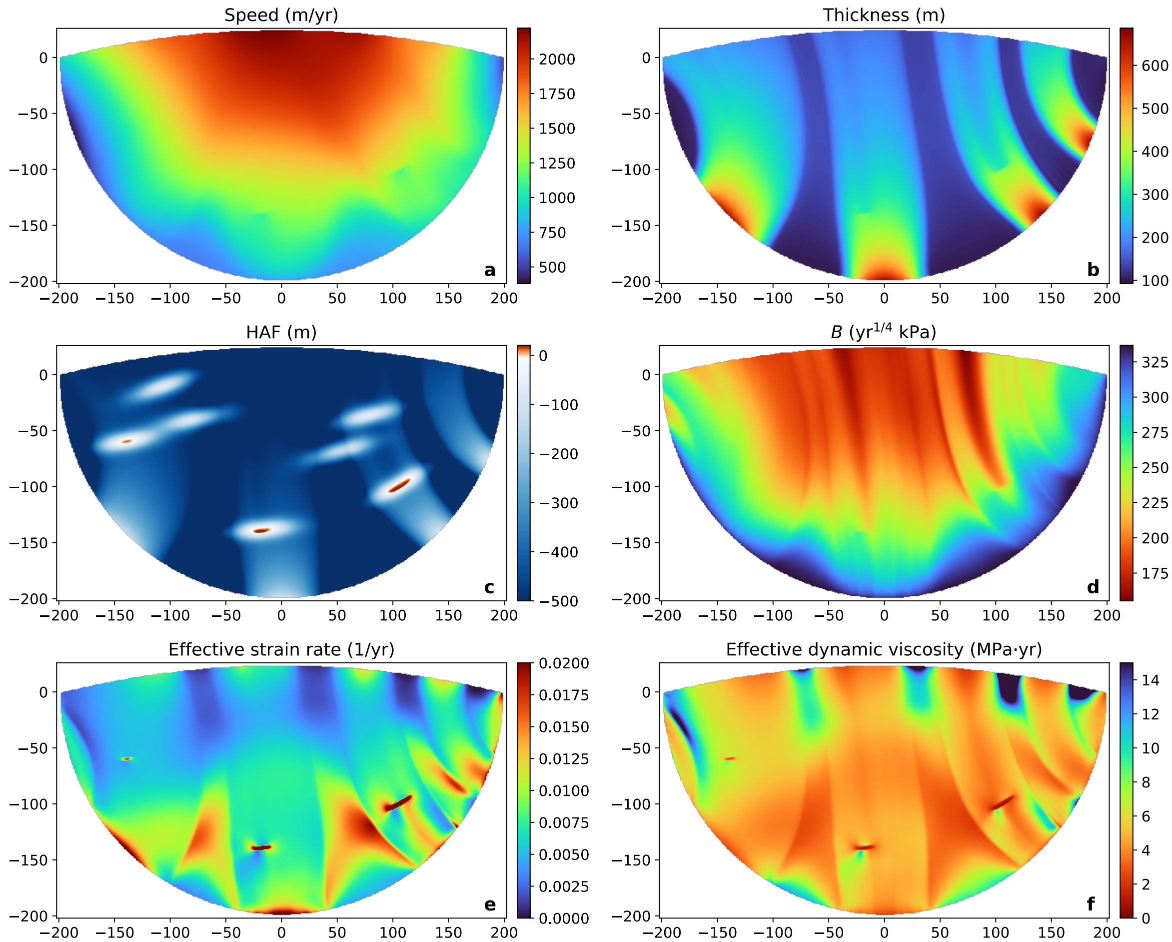

Fig. 3. 2D ice shelf with simulated damage evolution and pinning points. The simulation outputs shown are computed from 700 years of spinup in order to achieve steady state. The ice shelf is fed by four inlet ice streams, as evidenced by the flow speed (a) and ice thickness (b). Height-above-flotation (HAF) in (c) shows the location and orientation of the prescribed pinning points. The steady-state ice rigidity B (d) reflects damage accumulation due to shear margin weakening and ice thinning due to large strain-rates over the pinning points. The effective strain rate (e) and effective dynamic viscosity (f) are approximately inversely related and show strong shearing in the ice between the inlet flow, as well as over the pinning points. Strain rates are lower closer to the ice front. The effective viscosity exhibits a mix of long-wavelength variations within flow units and short-wavelength variations near the shear margins.

that results in a few pinning points where the flotation height is positive, i.e. the ice is actually grounded at these locations. Under the shallow-stream approximation, we prescribe a basal drag friction coefficient proportional to the flotation height such that friction is only non-zero for grounded ice. Such pinning points in the form of ice rumples are common in ice shelves in Antarctica. However, assuming a fully-floating ice shelf during inversion for rheological parameters will introduce errors into the inferred parameter field due to model mismatch. Therefore, by purposefully injecting modeling errors into the estimation procedure, we can assess how the two different cost functions and the estimated parameter uncertainties respond to such errors.

We first simulate the evolution of shelf velocity and thickness for roughly 500 years with a constant ice rigidity, B_0, corresponding to an ice temperature of -5° C, and a stress exponent of $n = 4$. Here, we choose $n = 4$ in order to evaluate the sensitivity of the rigidity inference to 2D ice stress variations that are more likely to be found in natural environments of fast-flowing ice (Bons and others, 2018; Millstein and others, 2022). After the first simulation stage, we apply a continuum damage mechanics model that modulates the rigidity field with an evolving damage factor, D, such that $B_D = (1 - D)^{-1} B_0$ (Borstad and others, 2013). This approach provides a physically realistic means to obtain a spatially-varying prefactor field with rheology-modifying processes such as shear weakening. We run the damage-enhanced model for an additional 200 years to achieve approximate steady-state. At the end of the simulation, we can observe substantial spatial variation in damage, where ice is nearly undamaged at the grounding line (due to a zero-damage boundary condition) and highly damaged near the ice front, at shear margins, and downstream of the pinning points. The dynamic effective viscosity field shows concentrated low viscosities near the pinning points and higher viscosities between the inlet ice streams where deformation rates are lower. Overall, the viscosities exhibit a mix of short- and long-wavelength features, which are mirrored in the effective strain rate field.

For recovery of the rigidity field, as discussed in Section , we explore both the conventional control method-based inversion and the variational inference approach based on the force balance objective, as well as a combination of the two where we use the inversion to set B_0 for the prior. For all approaches, we use the simulated ice surface elevation to compute ice thickness by assuming hydrostatic equilibrium (buoyancy). Over floating ice, the thickness values derived from buoyancy are identical to the simulated thickness, but over the pinning points, the actual thickness values are lower, which results in an overestimation of the driving stress variations using the buoyancy conversion (Figure S1). Furthermore, assuming flotation for the entire ice shelf will neglect the basal drag provided by the pinning points. The combined data and modeling errors will impact recovery of the prefactor field, which we explore shortly.

The control method inversion is again performed with `icepack`, using a Gauss-Newton solver to minimize a joint objective function that combines a velocity prediction error function and a regularization function based on the first-derivative of the rigidity field, B. For the variational inference problem, we select 20000 uniformly random locations on the ice shelf to extract velocity and thickness values to use as training data for the network f_ψ (feedforward network of four layers of 100 nodes each), which is only tasked with reconstructing the surface observations. We select an additional, independent set of 20000 random locations for training the VGP g_φ (with 750 inducing index points), which is tasked with predicting the parameters of the variational distribution $q(\theta)$. For all priors, we prescribe a lengthscale of 15 km, and for the prior with a uniform B_0, we use a value of $B_0 = 260$ yr$^{1/4}$ kPa. After training, we evaluate training performance by reconstructing the surface observations over the entire model domain (using f_ψ), as well as the predicted basal drag residual (using f_ψ and mean B as predicted by g_φ). For the variational inference predictions, the observation misfits and drag residual are minimal over most of the modeling domain but are higher over the two largest pinning points (Figure S3). The higher errors are a function of oversmoothing of the observations and model mismatch, which amounts to assuming ice is floating over the grounded pinning points. As a consistency check, we use the posterior samples of B to generate stochastic predictions of velocity using the standard forward model and find that velocity errors are generally less than 5% of the flow speed, with higher error values localized to the pinning points (Figure S4). We note that the velocity errors are commensurate with those from the conventional inversion.

A more detailed comparison of the recovery error for B between the control method inversion and variational inference reveals that the two methods are complementary. The control method inversion has the lowest overall error bias, but the areas where the errors are largest are systematically upstream of the pinning points (Figure 4). Since we assume all ice is floating for the forward model, the missing resistive stress provided by drag at grounded ice is compensated by artificially making the ice stiffer upstream of the pinning points, which acts to slow the ice down in a manner that allows the predicted velocities to match the observed velocities. In contrast, the B recovered by variational inference (which uses the SSA momentum balance as a forward model) shows larger errors directly over the pinning points, as well as in areas where ice is stagnant (low strain rate). Over the pinning points, the true rheology sharply varies from about 250 to 200 prior yr$^{1/4}$ kPa (Figure 3d). However, the prior lengthscale of 15 km encourages

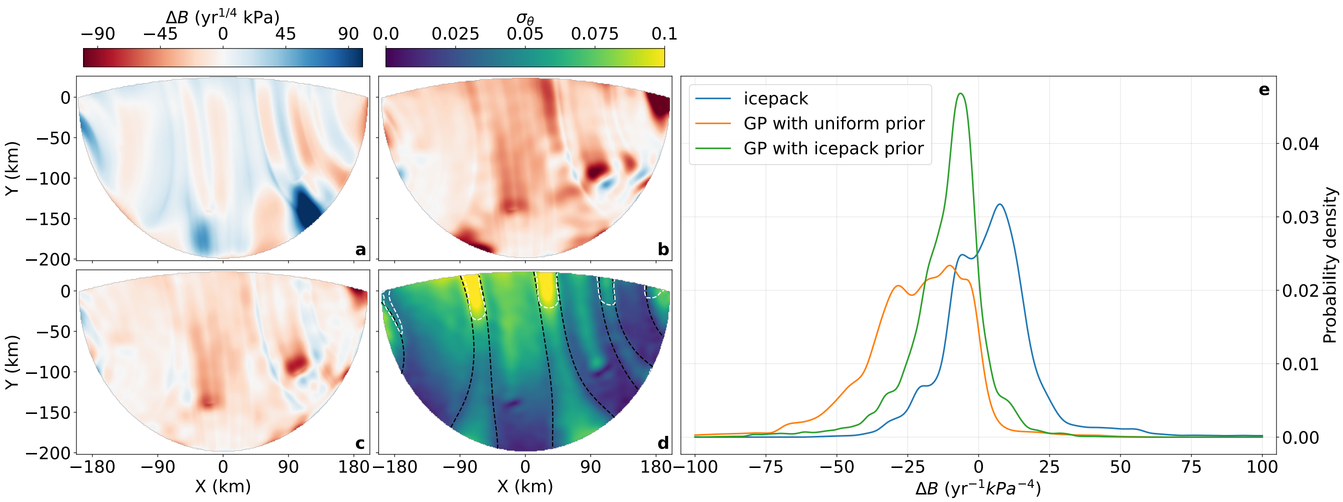

Fig. 4. Comparison of reconstruction errors for mean inferred ice rigidity between control method inversion and the proposed variational inference method. a) Error $(B - B_{\mathrm{true}})$ for control method inversion using `icepack`. b) Error for variational inference with a uniform B_0 field. c) Error for variational inference using the control method inversion for B_0. d) Inferred uncertainty for normalized rigidity parameter θ. Black dashed lines correspond to a thickness contour of 150 meters while the white dashed lines correspond to an effective strain rate contour of $10^{-2.6}$ yr^{-1}. e) Histograms of errors for different methods. Higher reconstruction errors and uncertainties are mostly concentrated in thinner ice and areas with with lower effective strain rates.

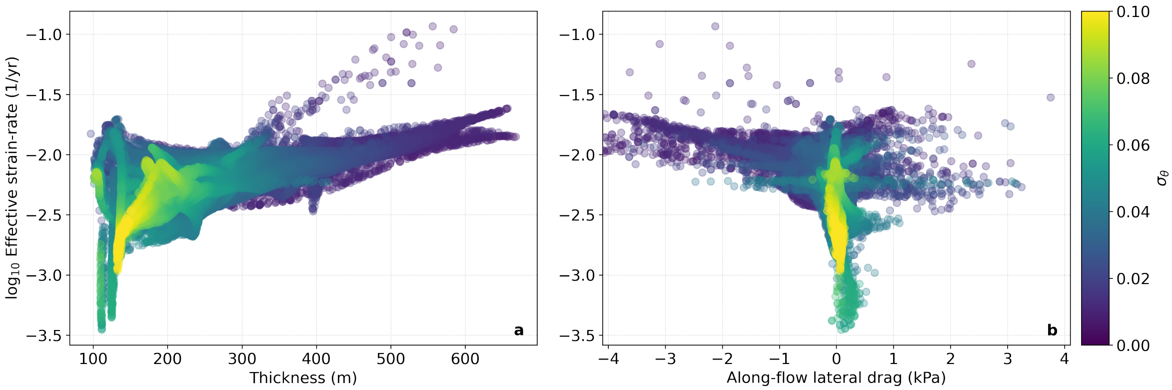

Fig. 5. Uncertainty for normalized rigidity θ vs. ice thickness, along-flow lateral drag, and effective strain rate for simulated 2D ice shelf. (a) Effective strain rate vs. ice thickness with colors corresponding to uncertainty in θ. (b) Same as (a) but for effective strain rate vs. along-flow lateral drag. Here, lateral drag is computed as the transverse gradients of the SSA momentum balance projected to the along-flow direction, where negative values denote flow resistance. While ice thickness is the first-order control on rigidity uncertainties, higher strain rates can reduce uncertainties in thinner ice. Positive lateral forces can also reduce uncertainties where effective strain rates are low.

spatially smoother fields of ice rigidity, which limits the dynamic range of ice stresses that can be modeled in order to satisfy the SSA momentum balance. Since the driving stress variations over the pinning points are overestimated due to the buoyancy assumption (Figure S1), the preferred solution is to smooth out all stress variations over the grounded ice in order to minimize the residual basal drag. Upstream of the pinning points and closer to the grounding line, the recovery errors are actually lower using variational inference as compared to the control method inversion. The spatial patterns in the recovery errors are similar to the patterns of residual basal drag (Figure S3). Finally, by using the control method inversion as the prior for variational inference, we can minimize much of the recovery errors closer to the ice front and in areas where strain rates are lower but flow speeds are still high, i.e. areas where the inversion has greater sensitivity (Figure 4c).

The predicted uncertainties for θ are consistent with the reconstruction errors: uncertainties are higher closer to the ice front where ice thicknesses are lower (as observed in the 1D case), as well as in more stagnant ice where strain rates are lower (Figures 4d, 5). In areas where ice is thinner but strain rates are higher (e.g., higher shear strain rate in the areas between the fast-flowing ice), the balance between extensional stresses and lateral drag also provides sufficient signal for reducing uncertainties. In a few isolated patches, even when effective strain rates are low and ice is relatively thin, slightly positive lateral forces that act as a "pull" on the ice can also reduce uncertainties (Figure 5). Over the pinning points, uncertainties are also higher where residual basal drag is higher. From a probabilistic perspective, the posterior means of θ over the pinning points are subject to a trade-off between being consistent with a high data likelihood (large absolute values of θ in order to satisfy zero basal drag) or with a high prior likelihood (θ close to 0). The optimal posterior distribution in this scenario is parameterized by mean θ values that compromise between the data and prior likelihoods while inflating the posterior standard deviations in order to "spread out" more probability mass. Overall, the uncertainty maps for θ are a useful diagnostic tool for locating potential modeling errors and providing a guide for optimal future data acquisition (acquiring data where posterior uncertainties are largest) and/or targeted inverse modeling to provide complementary, external estimates of model parameters to further reduce uncertainties (Figure S2).

WEST ANTARCTICA ICE SHELVES

We now apply our methods to select large ice shelves in West Antarctica, specifically the Larsen C Ice Shelf (LCIS), Filcher-Ronne Ice Shelf (FRIS), Ross Ice Shelf (RIS), and the combined Brunt Ice Shelf with Stancombe-Wills Ice Tongue and Riiser-Larsen Ice Shelf (B-SW-RL) (Figure 6). These ice shelves are fairly representative of shelf environments on the Antarctic coast and serve as a robust testing suite for several reasons. Firstly, they encompass a large area (48, 380, 440, and 68 $\times 10^3$ km^3 for LCIS, FRIS, RIS, and B-SW-RL, respectively), corresponding to a large number of effective modeling parameters in order to test the inference capacity of the VGP. Secondly, the ice shelves are subject to different flow and buttressing environments. Large ice rises in Larsen C have favored the formation of large rifts, the evolution of which are complicated by the presence of mechanically weak suture zones that likely contain large proportions of mechanically weak marine ice (Jansen and others, 2013; Kulessa and others, 2014; Borstad and others, 2017). Within Ross Ice Shelf (the largest ice shelf in Antarctica), a mix of ice rises, ice rumples, and large islands serve to create a heterogeneous flow environment involving localized grounding, rift formation, and shear margin weakening. Many of these pinning points lie in the western portion of the shelf off the Siple Coast, which drains much of the West Antarctic Ice Sheet through fast-flowing ice streams. Filchner-Ronne is also fed by several fast-flowing ice streams with large ice thicknesses, leading to larger driving stresses over the ice shelf with the highest overall flow speeds of the ice shelves examined here. The Brunt-Stancomb-Wills-Riiser-Larsen shelf complex (B-SW-RL) is subject to lower buttressing than Larsen C or Ronne-Filchner due to lack of embayments. However, within the Riiser-Larsen shelf are

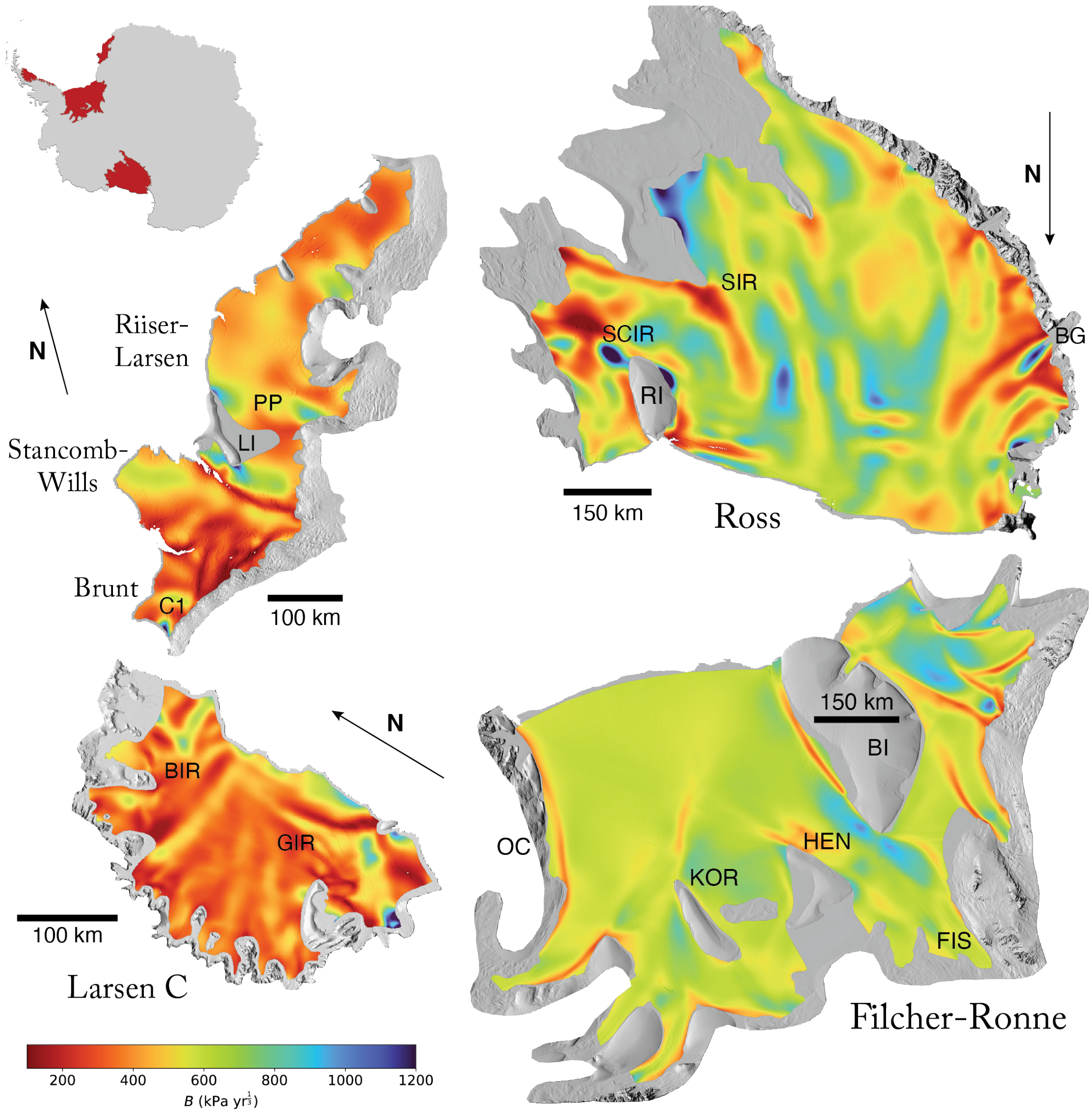

Fig. 6. Estimated mean ice rigidity B for West Antarctic ice shelves. Specific features in Ross Ice Shelf are Shirase Coast Ice Rumples (SCIR), Steershead Ice Rise (SIR), Roosevelt Island (RI), and Byrd Glacier (BG). At Filcher-Ronne Ice Shelf are Korff (KOR) and Henry (HEN) ice rises, Berkner Island (BI), Foundation Ice Stream (FIS), and Orville Coast (OC). At Larsen C are Bawden (BIR) and Gipps (GIR) Ice Rises. At Brunt-Stancomb-Wills-Riiser-Larsen is Chasm 1 (C1), Lyddan Island (LI), and an unnamed pinning point (PP). Inset at the top left shows the location of the ice shelves in Antarctica. Overall, areas of soft ice are inferred at shear margins and large surface crevasses, while areas of stiffer ice are associated with thick ice in compressional zones.

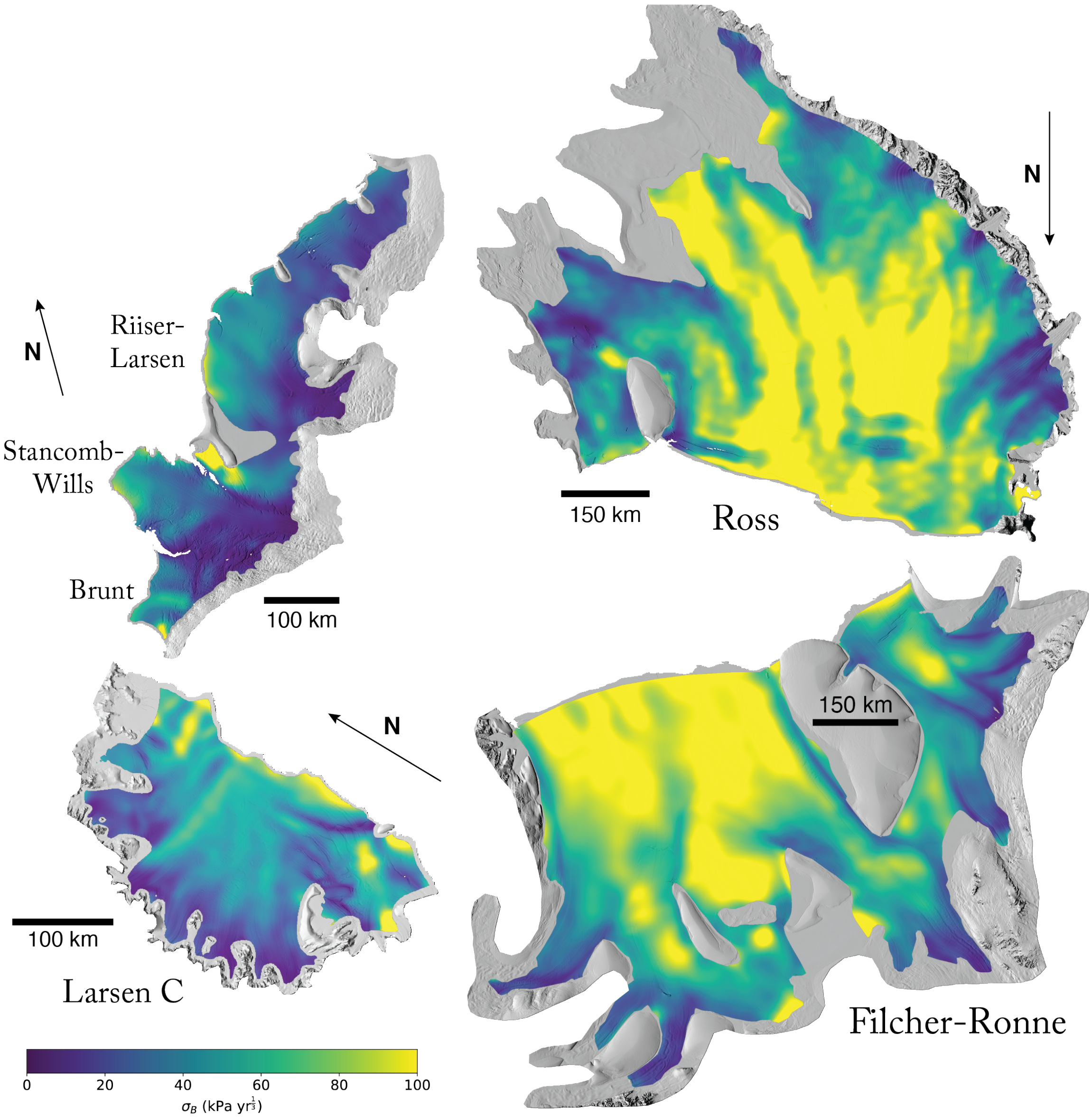

Fig. 7. Estimated 1-σ B uncertainties for West Antarctic ice shelves. Uncertainties are generally larger for higher B values (scale-dependence) and for areas with thinner ice and lower driving stresses. Uncertainties tend to be lower closer to the grounding line.

a few prominent pinning points that do provide limited buttressing but also serve as potential areas of model mismatch, similar to the synthetic ice shelf we previously investigated. Additionally, much of the ice in the Stancomb-Wills ice tongue is more loosely packed, leading to large surface gradients at the edges of individual ice units that are not well-matched to velocity variations.

For RIS and B-SW-RL, we use the MEaSUREs velocity mosaic (Rignot and others, 2011; Mouginot and others, 2012), which combines speckle tracking of SAR images from various satellite platforms with feature tracking of Landsat 8 images and has a nominal temporal coverage between 2009 - 2016. For LCIS and FRIS, we use a 2020 annual velocity mosaic provided by ITS_LIVE, which is derived from feature tracking of Landsat 7 and 8 images over Antarctica (Gardner and others, 2019). From a visual inspection, we found that the ITS_LIVE mosaic exhibited fewer velocity artifacts for LCIS and FRIS, whereas the MEaSUREs mosaic exhibited fewer artifacts over B-SW-RL and provided full coverage over RIS. Ice thickness data are derived from BedMachine V2 (Morlighem and others, 2020), which combines radar-estimated thickness profiles with mass conservation constraints and firn corrections in order to obtain continuous thickness maps. Surface elevations are then recovered assuming buoyancy. While the nominal year for the thickness data is 2015, the correspondence between the velocity and thickness data are sufficient for the spatial resolution of our analysis (assuming an upper bound of $\approx$ 5 km of motion for feature advection).

For all velocity and thickness rasters, we first perform a void-filling operation that uses a spring-based PDE constraint to fill in missing data (D'Errico, 2012). The rasters are then filtered to $\approx$10-15 times the average ice thickness using a Savitzky-Golay filter in order to remove high-frequency components not resolvable by the SSA force balance. As with the simulated ice shelf, we first invert for B using `icepack` in order to optimize a cost function combining a velocity misfit term (weighted by the formal uncertainties for the velocity estimates) and a regularization term based on first-order spatial gradients to encourage smoother solutions. A penalty parameter controlling the relative contribution of the regularization term is selected with a standard L-curve analysis, independently for each ice shelf. For each ice shelf, we use feedforward neural networks with four layers of 100 nodes each and VGPs with 600–900 inducing index points. Finally, we use the estimated B field as the prior for variational inference, setting the prior variance for θ to 0.2^2.

To a first-order approximation, ice is inferred to be stiffer for FRIS and RIS than for LCIS and BWSRL, and average rigidity values for LCIS are the lowest of the four (Figure 6). These first-order trends are well-matched by modeled ice shelf surface temperatures where temperatures for FRIS are generally around

-25 to -30 °C, whereas for LCIS they range from -15 to -10 °C (Figure S6). However, all ice shelves exhibit significant spatial variability in inferred ice rigidity beyond surface temperature variations. For FRIS, the estimated mean B field is broadly consistent with results from prior studies (e.g., MacAyeal and others, 1998; Larour and others, 2005). Ice is inferred to be substantially softer in the shear margins where strong lateral shearing leads to viscous dissipation and elevated ice temperatures. These shear margins are prominent in the Ronne Ice Shelf where fast-flowing floating ice is in contact with rock (along the Orville coast and Berkner Island) or stagnant ice, as is the case downstream of the Korff Ice Rise. As discussed in Larour and others (2005), larger basal melt rates on the northern tip of the Henry Ice Rise are coincident with softer ice. Within the Filchner Ice Shelf, lower overall values of B indicate softer ice, again in the shear margins where ice streams flow onto the shelf and are in contact with stagnant ice. A large lateral surface crevasse close to the ice front is also associated with higher strain rates and softer ice. We can also observe localized regions of substantially stiffer ice, such as downstream of the Foundation Ice stream and upstream of the Korff and Henry Ice Rises. These regions are associated with larger driving stresses (Figure S5) such that ice is inferred to be stiffer in order to provide enough resistive stresses to balance those driving stresses. Ice is also inferred to be stiffer closer to the grounding line where colder ice is advected by the ice streams.

Similar to FRIS, the ice in the central portions of RIS are inferred to be more rigid, likely due to relatively cold surface temperatures of -20 °C. However, we can also observe zones of softer ice near shear margins and localized areas of grounding. At the inlet of the Byrd Glacier to the west, prominent shear margins separating the fast-flowing inlet ice from more stagnant shelf ice are coherent for more than 300 km downstream of the grounding line (Figure S5), which results in substantial shear weakening. In the central trunk of the Byrd Glacier inlet, the reduction in flow speed as the ice flows onto RIS leads to enhanced compressional stress and thickening of the ice, leading to inferred higher B values. On the east side of RIS, the Shirase Coast Ice Rumples (SCIR) at the outlet of the MacAyeal and Bindschadler Ice Streams significantly modify the flow field and ice thickness due to grounding of the ice, consistent with the simulated pinning points in Section . Thinning of ice downstream of SCIR and diversion of the shear margins towards Roosevelt Island (RI) are both dynamical effects that modify the buttressing capability of ice in this region (Still and others, 2019; Still and Hulbe, 2021). In our inferred B field, the ice covering the rumples is inferred to be softer while the downstream ice connected to RI is inferred to be stiffer. Alternatively, the ice upstream of Steershead Ice Rise (SIR) is near-stagnant, leading to very high inferred values for B. Downstream of SIR is a streakline of thin ice coincident with the shear margin of the inlet of MacAyeal and Bindschadler Ice Streams, leading to a narrow zone of soft ice that persists nearly all the way to the ice front.

At LCIS, the softest ice is inferred within highly localized areas corresponding to surface crevassing, including the large rift originating from the Gipps Ice Rise (Khazendar and others, 2011; Larour and others, 2021). It is likely that some fraction of the inferred softness is due to not explicitly including rifts (geometrically and dynamically) within the ice flow model, which can reproduce a significant proportion of the observed strain rates with active opening/closing of rifts (Larour and others, 2021). As is the case with FRIS, stiffer ice is inferred near the grounding line where colder and thicker ice is advected downstream by the inlet ice streams. Within the ice shelf, areas in between faster flowing ice correspond to thinner ice and higher strain rates, resulting in softer ice. Unlike FRIS, the proximity of the fast flowing inlet ice streams with one another limits the areal extent of stagnant ice over Larsen C. High effective strain rates between ice streams are aligned with the initiation of suture zones where mechanically weak marine ice (sourced from warmer ocean water) has been observed to accumulate at the base of LCIS (Kulessa and others, 2014). The initial portion of the suture zones within approximately 20-30 km downstream of promontories and peninsulas are associated with inferred softer ice. Upstream of the Bawden Ice Rise (BIR), strain rates are substantially lower and correspond to larger inferred B values. Here, the correspondence between large fractures and a simulated confluence of meltwater plumes is hypothesized to stimulate abundant accretion of marine ice, which can actually lead to ice stiffening (Khazendar and others, 2011).

Finally, for B-SW-RL, ice is inferred to be substantially softer in the mélange area that separates the Brunt Ice Shelf from the Stancomb-Wills Ice Tongue, as well as in the mélange that separates the latter from the Riiser-Larsen Ice Shelf. These areas, which contain a heterogeneous mixture of marine ice, sea ice, and ice shelf debris, have previously been inferred to exhibit lower rigidity values (within a continuum mechanics model) and act to bind large ice fragments to the coast (Khazendar and others, 2009). Since the mélange is less coherent than meteoric ice advected from the ice streams, it deforms readily and corresponds to high strain-rates. Additionally, prominent surface crevasses throughout B-SW are also associated with softer ice, including several transverse rifts close to the grounding line of Brunt Ice Shelf and a frontal rift separating the northeastern corner of Brunt Ice Shelf from the Stancomb-Wills Ice Tongue. Since the nominal temporal coverage of the MEaSUREs velocity data is 2009 - 2016, the Halloween Crack has not yet initiated (De Rydt and others, 2019). At the southern edge of Brunt Ice Shelf at the base of Chasm 1, ice is actually inferred to have high mean B, but since uncertainties are large here (Figure 7), we consider this to be a smoothing artifact stemming from larger thickness errors near the large rifts. Upstream of the prominent pinning point on the Riiser-Larsen Ice Shelf (PP in Figure 6), ice is inferred to be stiffer, similar to what we observed with the simulated pinning points in Section as a compensation for unmodeled basal drag. The thinner ice downstream of the pinning point is correspondingly inferred to be softer. We do note that the orientation of the flow field relative to the pinning point is more oblique than that of our simulated shelf, which likely is the source of the more complex strain rate pattern adjacent to the pinning point (Figure S5). Finally, upstream of Lyddan Island in the mélange at the eastern edge of Stancomb-Wills, ice is inferred to have high rigidity, but as this area corresponds to both low strain rates and low driving stress, the uncertainty in rigidity is very large.

Posterior Predictive Distributions and Ice Shelf Buttressing

After obtaining the variational distribution that best approximates the posterior distribution for the ice rigidity, we can compute a posterior predictive distribution for any quantity or forward model that depends on the rigidity. The most straightforward way to accomplish this is to generate random samples from the variational distribution and pass each sample through the forward model of interest, i.e. Monte Carlo approximation. For example, one could perform a dynamic perturbation analysis on specific ice shelves by applying some form of stress perturbation at the ice front (calving event, gain/loss of buttressing sea ice, etc.) and running prognostic simulations for different realizations of the rigidity, sampled from the posterior distribution. This type of analysis has been performed in many studies to assess sensitivity of ice shelves to changing climate conditions (e.g., Schlegel and others, 2018; Nias and others, 2019), but usually the rigidity field is varied by choosing some uniform upper and lower bound guided by expected temperature variations or other *a priori* knowledge on creep mechanisms. By instead using the posterior distribution to draw samples of the rigidity, we automatically incorporate information derived from surface observations while also allowing known physical laws (e.g., SSA equations) to induce realistic covariances between values of the rigidity over finite length scales. In other words, the combined information from data and flow equations results in more realistic samples of physical parameters consistent with all known knowledge.

Since one of the most important physical implications of ice shelf rheology is the amount of buttressing applied to inland grounded ice, we use the variational distribution for B to compute the distribution of maximum buttressing factors following Fürst and others (2016). The buttressing factor for a given location on an ice shelf is the ratio between the normal force exerted by the ice shelf on upstream ice in a given horizontal direction to the expected stress applied by the ocean to upstream ice if the ice shelf was removed to that location. By performing systematic calving simulations where ice is removed from an ice shelf up to different buttressing factor isolines, the increase in ice flux across the ice front or grounding line can be predicted for various buttressing factors (Fürst and others, 2016). The buttressing factor above which ice flux is projected to rapidly increase then serves as a buttressing threshold for a given ice shelf. The isoline corresponding to the threshold can then delineate regions of "passive" shelf ice (PSI), defined as ice that can be removed without significantly altering the flow dynamics of the adjacent ice. As the normal force in the buttressing factor is computed from the ice stress tensor, which itself depends on the rigidity B to estimate the stress components, the buttressing factor will be subject to random variations consistent with the posterior samples of B. We can therefore estimate the expected variation in PSI consistent with the surface observations. In order to estimate a more realistic estimate of PSI area specific to calving, we only include buttressing factor isolines that form polygons that intersect the ice front, meaning we exclude areas of isolated PSI closer to the grounding line.

The buttressing thresholds originally presented by Fürst and others (2016) corresponded to flux increases across the ice front, leading to threshold values of 0.3 - 0.4 for the ice shelves investigated here. Alternatively, thresholds defined for increased ice flux across the grounding line are found to be a better predictor for ice shelf stability in response to instantaneous calving events (Reese and others, 2018; Mitcham and others, 2022). These buttressing values tend to range from 0.8 - 0.9. For the purposes of comparison with the result of Fürst and others (2016), we use a lower threshold of 0.4 roughly corresponding to a step increase in flux across the ice front. Due to slight biases between our inferred mean B fields and the fields estimated by Fürst and others (2016), our threshold value of 0.4 is slightly higher than that used by Fürst and others (2016) in order to roughly match the PSI regions in that study.

We observe variations in PSI that lie roughly within the bounds computed from $\pm$ 10 % variation of the mean B, following Fürst and others (2016) (Figure 8). However, we can observe additional spatial and statistical patterns beyond the simple $\pm$ 10 % variations. For the ice shelves that are laterally confined by embayments, there are a significant number of samples of the PSI boundary that exceed the upper and lower bounds. Over Larsen C, the PSI boundary samples are slightly skewed towards lower PSI areas. However, several posterior samples of B actually connect passive ice centered on the rift originating from

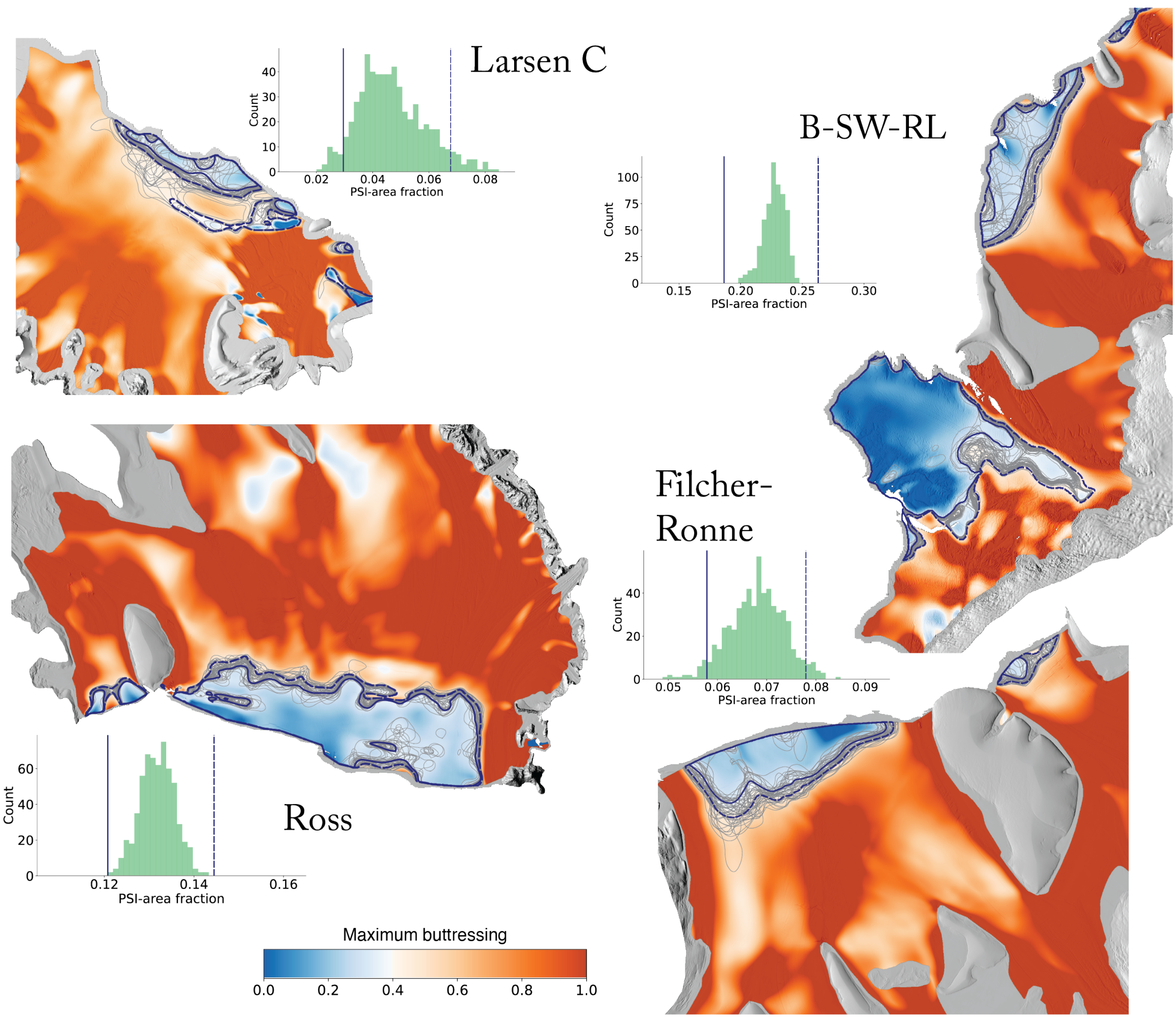

Fig. 8. Stochastic analysis of maximum buttressing factor for West Antarctic ice shelves, following Fürst and others (2016). Background 2D buttressing fields are computed from the mean B inferred from variational inference for each ice shelf. The colormap is constructed to highlight a threshold buttressing value of 0.4, which roughly corresponds to a step increase in ice flux across the ice front for removal of ice up to the 0.4 buttressing isoline. Thus, blue areas correspond to “passive” ice. The thick solid and dashed dark blue lines correspond to the 0.4 isoline for a $\pm$ 10% variation of B about the mean, respectively. Thin gray lines correspond to the 0.4 isoline for B samples from the variational posterior distribution. For each ice shelf, a histogram is shown of the passive ice shelf area estimated from samples from the posterior, along with the same $\pm$ 10% lower and upper bounds shown in the maps.

GIR to passive ice at the ice front, which increases total PSI area and slightly reduces the vulnerability of Larsen C to ice loss. Over FRIS and Ross, the PSI distribution is more symmetrical, although the former has a long tail of lower PSI areas, which correspond to a slight increase in vulnerability of those shelves to ice loss. Finally, over B-SW-R, the distribution of PSI is near-symmetric and lies well within the $\pm$ 10 % bounds. However, the difference in spatial extent between the $\pm$ 10 % bounds is larger than for the other ice shelves, particularly for the Stancomb-Wills ice tongue, which indicates a greater sensitivity to variations and uncertainties in inferred ice rigidity. This sensitivity is likely reflective of the lack of lateral confinement and drag and highlights the importance of embayment geometry on ice shelf buttressing force. Overall, these results demonstrate that calibration of ice shelf rigidity and associated uncertainties using surface data can both inflate/deflate predictive uncertainties and needs to be performed on a shelf-by-shelf basis.

DISCUSSION

We demonstrated our proposed physics-informed variational inference framework by estimating the posterior distribution of ice rigidity for synthetic and large-scale ice shelves in Antarctica. The variational inference scheme produces posterior distributions of rigidity that agree well with those estimated by MCMC methods while providing a scalable approach for exploring uncertainties in parameter fields and forward predictions. We now briefly discuss potential avenues for further exploration of ice rheological parameters using distributions of B, as well as future algorithmic and computational improvements.

Uncertainties in ice rigidity propagated to flow law parameters

In this work, we focused on estimating the variational distribution for ice rigidity, B, and demonstrate how the the inferred uncertainties can be used to form predictive distributions on a derived buttressing factor (Section). However, B was defined using the form of Glen's Flow Law in Equation 1, which aggregates multiple physical factors into a single prefactor. The prefactor can be disaggregated using an Arrhenius-type relation with the following form (using the convention that $B = A^{-1/n}$) (Cuffey and Paterson, 2010):

$$A = EA_0 \exp\left\{\frac{-Q_c}{R}\left(\frac{1}{T} - \frac{1}{T_0}\right)\right\}, \tag{18}$$

where A_0 is a reference prefactor value, R is the ideal gas constant, T is temperature, $T_0 \approx -10°\text{C}$ is a transition temperature corresponding to a switch in the activation energy for creep, Q_c, and E is an enhancement factor that depends on the ice crystallographic fabric, grain size, damage, and water and impurity content. Therefore, it is possible to decompose the inferred distribution of B into probability distributions for the unknown parameters in the above relation (all parameters except R). However, such a decomposition is highly ill-posed and only possible if relatively strong prior constraints are available for the parameters. For example, ice temperatures can be measured at select locations and modeled independently with an appropriate thermomechanical model. The spatial variations in E are likely to be highly correlated with the deformation mode (e.g., simple shear vs. extension), which can be well-approximated from surface strain-rates. On the other hand, the activation energy Q_c, which is temperature dependent through T_0, is likely to be relatively uniform within the two separate temperature regimes partitioned by T_0. The differences in expected spatial variation can thus be used as prior constraints when forming the joint posterior distribution of the parameters in Equation 18.

Influence of modeling errors

Models of complex physical systems are generally incomplete and do not fully represent all physical processes found in natural settings. Modeling errors will therefore affect inference of parameter values and associated posterior distributions. In the case of ice shelves, we have represented ice flow in a continuum mechanics framework with a momentum balance based on the SSA, which assumes that the vertical profile of ice rigidity for an ice column can be represented by its depth-averaged value and that all ice is floating within the ice shelf. The former assumption likely results in inconsequential prediction errors since ocean water provides minimal drag to the base of ice shelves. The assumption of floating ice is violated in areas where ice is locally grounded, which in Section we observed can cause a localized bias in inferred rigidity values around and upstream of the grounded area. These biases arise from the uniform uncertainties, σ_{τ_b}, we prescribed in the likelihood model in Equation 9. In reality, these uncertainties should be scaled according to expected variations in residual basal drag, which are likely to be informed by estimates of flotation height. A simple scaling of the uncertainties follows from consideration of the sensitivity of the forward model to the assumed basal drag value, which is nominally zero over ice shelves. Since the forward model used here directly uses the SSA momentum balance, the sensitivity matrix for basal drag is identity, and the total prediction uncertainty arising from drag uncertainties is the drag uncertainty itself (Duputel and others, 2014). This approach is appropriate when the primary objective is physical interpretation of the distribution of rigidity values (as discussed in the previous section). However, if the primary goal is to use the posterior distribution of rigidity to construct ensembles of ice flow model runs (e.g., to estimate range of probable contributions to sea level rise), then a bias in the distribution for rigidity is acceptable since an increase in ice rigidity will compensate for the missing basal drag for grounded ice.

Another source of modeling uncertainty comes from our use of a conventional inverse method to pre-compute a B_0 field to be used as a prior mean. This strategy nominally reduces uncertainties in ice rigidity near the ice front (Figure S2). However, the conventional inversion requires specification of a dynamic boundary condition at the ice front based on the hydrostatic pressure provided by the ocean water. In areas where considerable sea ice has formed at the ice front, uncompensated buttressing stress provided by the sea ice will lead to biased estimates of B_0, which can be considered as an additional source of modeling uncertainty. One strategy to account for such uncertainties is to treat B_0 as a hyperparameter in order to formulate a hyperprior for the rigidity such that $p(B) = \int p(B|B_0)p(B_0)dB_0$. The distribution $p(B_0)$ (resulting only from uncertainties in the dynamic boundary condition) can be pre-estimated by repeating the control method inversion for different values of buttressing stress at the ice front.

Integration with numerical ice flow models

The SSA momentum balance is the basis of the forward model for our method, which differs from the forward model of predicted ice velocities used in traditional control-method-based inversions and previous studies investigating Bayesian methods for parameter estimation for ice dynamics (Section). If the surface data are noise-free and the boundary conditions at the grounding line and ice front are known perfectly, the two different forward models would result in identical point estimates of ice rigidity. However, even in this ideal scenario, posterior inference with the two different forward models would lead to uncertainties with different spatial variations due to different model sensitivities. The velocity-based forward model is most sensitive to rigidity variations where velocities are higher, usually closer to the ice front. On the other hand, the momentum-based forward model is most sensitive to rigidity variations closer to the grounding line where driving stresses are higher, as well as in high strain-rate regions where driving stresses are lower (Figure 5). One possible avenue for future work is to integrate the variational inference scheme of Brinkerhoff (2022), which uses a velocity-based forward model, with the methods presented here in order to provide complementary model sensitivities. Furthermore, recent advances in deep learning-based surrogate modeling could significantly improve the computational efficiency of velocity-based forward models by replacing expensive forward solves with much cheaper neural network predictions (Jouvet and others, 2021).

General uncertainty quantification in physics-informed machine learning and computational considerations

In this work, we focused on estimating a variational distribution for the ice rigidity B, conditional on observations of ice surface velocity and elevation and the SSA governing equations for ice flow. However, the methods presented here are directly applicable to other physics-informed machine learning problems focused on solving inverse problems and quantifying uncertainties for inferred parameter fields (e.g., Raissi and others, 2020). There are two main requirements for direct application of the variational inference methods: 1) The parameter field of interest must be predictable at arbitrary input coordinates both within and outside of the training data; and 2) the physics-informed loss that functions as a forward model must be separable, i.e. physics losses at a given input must be computable independent of the other inputs. For the latter requirement applied to physics losses derived from PDEs, gradients need to be computable at arbitrary inputs, which is generally straightforward with automatic differentiation. Furthermore, if temporal gradients are computable, then variational inference can be extended to time-dependent PDEs. For example, the variational inference framework could be used to infer a spatially-varying thermal diffusivity for a model governed by the heat equation. Time-dependent observations of temperature profiles would be reconstructed by a neural network, $T(x, y) = f_\psi(x, y, t)$, and a VGP would be trained to generate samples of the thermal diffusivity at arbitrary spatial coordinates, $\alpha(x, y) \sim \mathcal{VGP}_\varphi(x, y)$.

From a computational efficiency standpoint, the VGP used for the variational distribution is a marked improvement from standard GPs, but the need to learn a full-rank Gaussian distribution at the inducing points still prevents the VGP from being applicable to very large spatial domains (or, equivalently, model domains where high-spatial resolution of parameter fields is desired). As the number of inducing points exceeds $\approx$1000, computational and memory requirements become excessive and training efficiency drops dramatically. While training efficiency of VGPs could be improved through the use of second-order optimizers (e.g., Newton- or quasi-Newton-based optimizers), joint training of VGP and neural network parameters would become intractable since neural networks tend to have a significantly larger number of parameters. Therefore, future work must involve the development of alternative models for variational distributions that are suitable for large effective model dimensions.

The variational posterior inference presented here shares many of the training techniques developed for variational autoencoders (VAEs) (Kingma and Welling, 2013). In that work, posterior inference is performed on a generic latent variable that best represents a low-dimensional projection of independent factors of variation in high-dimensional datasets. For physical inverse problems, the latent variable corresponds to the parameter we are trying to infer. The encoder in the VAE framework is the machine learning model used to predict the parameter statistics at arbitrary inputs (e.g., the VGP used here) while the decoder is simply the forward model. With this interpretation, we can recognize potential avenues for improving training efficiency for the variational distribution. Neural network architectures that specialize in learning spatial relationships in high-dimensional images, e.g. convolutional neural networks (LeCun and others, 2010), vision transformers (Dosovitskiy and others, 2020), or Fourier neural operators (Li and others, 2020), are proven to generalize well in variational autoencoder frameworks (e.g., Tomczak and Welling, 2018). Thus, by replacing both the neural network used to predict the surface observations and the VGP used for representing the posterior distribution with a specialized neural network architecture, it may be possible to efficiently model the variational parameters (mean and covariance values) for high-dimensional model domains. Alternatively, one could perform inference on latent variables that are low-dimensional representations of the parameter of interest (e.g., Brinkerhoff, 2022). In that case, computational efficiency can be improved by discovering the most parsimonious latent space that satisfies a certain reconstruction accuracy threshold.

CONCLUSIONS

In this work, we present a framework for inferring the posterior distribution of ice rheology for large ice shelves in West Antarctica. Motivated by recent advances in physics-informed machine learning and variational inference, the framework utilizes neural networks to reconstruct spatially-dense observations of ice surface velocity and thickness, which allows for mesh-free evaluation of surface variable values and associated spatial gradients. At the same time, we task a variational Gaussian Process to predict the mean and covariance of ice rheological parameters for arbitrary spatial coordinates. By using the momentum balance for ice-flow appropriate for ice shelves, we formulate a mapping from parameters (rheology) to observables (residual momentum) that is inherently parallelizable and allows for joint training of the neural networks and variational Gaussian Process using stochastic gradient descent. The training objective utilizes a variational approximation to Bayesian inference, which provides an explicit way to encode prior rheology information in the form of spatial lengthscales (to modulate smoothing of the inferred rheology field) and range of variation relative to a reference field. For the latter, we show that using a conventional inversion method to estimate a prior mean field can reduce reconstruction errors, which demonstrates a potentially favorable approach to exploring uncertainties in large-scale ice flow models without injecting them into computationally expensive MCMC samplers.

Using these methods, we demonstrate posterior inference of ice rheology for synthetic 1D and 2D ice shelves. We find that rheological uncertainties are lowest where driving stresses and strain-rates are higher, corresponding to larger components of the momentum balance and higher levels of ice deformation, which implies more information about ice rheology. Using the synthetic 2D ice shelves, we also demonstrate how the momentum balance-based forward model can help reduce biases in inferred ice rigidity near areas of localized grounding where the shallow-shelf approximation of the momentum balance is violated. Inference of the distribution of ice rigidity values for select West Antarctic ice shelves reveal a wide range of spatial patterns consistent with highly heterogeneous flow environments. Generally, we find softer inferred ice in shear margins, near pinning points, and around visible surface crevasses. Conversely, ice is inferred to be stiffer where bulk ice temperatures are lower and where compressional stresses result in thickening of ice, such as upstream of certain ice rises or where fast-flowing ice streams flow onto slower shelf ice. Finally, using the posterior covariances of rigidity, we generate stochastic predictions of buttressing factors for the West Antarctic ice shelves and show how different flow environments can result in different ranges of passive shelf ice areas, as well as different levels of non-Gaussian behavior. These results demonstrate the utility of site-specific posterior inference for predictive modeling as opposed to assuming uniform lower and upper bounds for an entire ice sheet.

ACKNOWLEDGEMENTS

This research was partially supported by NSFGEO-NERC grant 1853918, the John W. Jarve (1978) Seed Fund for Science Innovation, and the Earl A Killian III (1978) and Waidy Lee Fund. **Code and data availability:** ITS_LIVE velocity data can be downloaded at `https://nsidc.org/apps/itslive/`. MEaSUREs velocity data can be downloaded at `https://nsidc.org/data/NSIDC-0484/versions/2`. BedMachine V2 thickness data can be downloaded at `https://nsidc.org/data/NSIDC-0756`. Example scripts for

variational inference for 1D and 2D ice shelves can found at `https://github.com/bryanvriel/physics-informed-vi`. Neural network and variational Gaussian Process models were written using TensorFlow (`https://www.tensorflow.org`) and TensorFlow Probability (`https://www.tensorflow.org/probability`).

REFERENCES

Albergo MS, Boyda D, Hackett DC, Kanwar G, Cranmer K, Racanière S, Rezende DJ and Shanahan PE (2021) Introduction to normalizing flows for lattice field theory. *arXiv preprint arXiv:2101.08176*

Aschwanden A, Bartholomaus TC, Brinkerhoff DJ and Truffer M (2021) Brief communication: A roadmap towards credible projections of ice sheet contribution to sea level. *The Cryosphere*, **15**(12), 5705–5715 (doi: 10.5194/tc-15-5705-2021)

Babaniyi O, Nicholson R, Villa U and Petra N (2021) Inferring the basal sliding coefficient field for the stokes ice sheet model under rheological uncertainty. *The Cryosphere*, **15**(4), 1731–1750 (doi: 10.5194/tc-15-1731-2021)

Blei DM, Kucukelbir A and McAuliffe JD (2017) Variational inference: A review for statisticians. *Journal of the American Statistical Association*, **112**(518), 859–877 (doi: 10.1080/01621459.2017.1285773)

Bölcskei H, Grohs P, Kutyniok G and Petersen P (2019) Optimal approximation with sparsely connected deep neural networks. *SIAM Journal on Mathematics of Data Science*, **1**(1), 8–45

Bons PD, Kleiner T, Llorens MG, Prior DJ, Sachau T, Weikusat I and Jansen D (2018) Greenland Ice Sheet: Higher nonlinearity of ice flow significantly reduces estimated basal motion. *Geophysical Research Letters*, **45**(13), 6542–6548 (doi: 10.1029/2018GL078356)

Borstad C, McGrath D and Pope A (2017) Fracture propagation and stability of ice shelves governed by ice shelf heterogeneity. *Geophysical Research Letters*, **44**(9), 4186–4194 (doi: 10.1002/2017GL072648)

Borstad CP, Rignot E, Mouginot J and Schodlok MP (2013) Creep deformation and buttressing capacity of damaged ice shelves: theory and application to Larsen C ice shelf. *The Cryosphere*, **7**(6), 1931–1947 (doi: 10.5194/tc-7-1931-2013)

Brinkerhoff DJ (2022) Variational inference at glacier scale. *Journal of Computational Physics*, **459**, 111095, ISSN 0021-9991 (doi: 10.1016/j.jcp.2022.111095)

Cuffey KM and Paterson WSB (2010) *The Physics of Glaciers*. Academic Press

Cybenko G (1989) Approximation by superpositions of a sigmoidal function. *Mathematics of control, signals and systems*, **2**(4), 303–314

De Rydt J, Gudmundsson GH, Nagler T and Wuite J (2019) Calving cycle of the Brunt Ice Shelf, Antarctica, driven by changes in ice shelf geometry. *The Cryosphere*, **13**(10), 2771–2787 (doi: 10.5194/tc-13-2771-2019)

D'Errico J (2012) inpaint_nans, matlab central file exchange. Accessed June 2021 at https://www.mathworks.com/matlabcentral/fileexchange/4551-inpaint_nans

Dillon JV, Langmore I, Tran D, Brevedo E, Vasudevan S, Moore D, Patton B, Alemia A, Hoffman M and Saurous RA (2017) Tensorflow Distributions. *arXiv preprint arXiv:1711.10604*

Dosovitskiy A, Beyer L, Kolesnikov A, Weissenborn D, Zhai X, Unterthiner T, Dehghani M, Minderer M, Heigold G, Gelly S and others (2020) An image is worth 16x16 words: Transformers for image recognition at scale. *arXiv preprint arXiv:2010.11929*

Duputel Z, Agram PS, Simons M, Minson SE and Beck JL (2014) Accounting for prediction uncertainty when inferring subsurface fault slip. *Geophysical Journal International*, **197**(1), 464–482 (doi: 10.1093/gji/ggt517)

Ernst OG, Mugler A, Starkloff HJ and Ullmann E (2012) On the convergence of generalized polynomial chaos expansions. *ESAIM: Mathematical Modelling and Numerical Analysis*, **46**(2), 317–339

Fürst JJ, Durand G, Gillet-Chaulet F, Tavard L, Rankl M, Braun M and Gagliardini O (2016) The safety band of Antarctic ice shelves. *Nature Climate Change*, **6**(5), 479–482 (doi: 10.1038/nclimate2912)

Gardner A, Fahnestock M and Scambos T (2019) ITS_LIVE regional glacier and ice sheet surface velocities. *Data archived at National Snow and Ice Data Center* (doi: 10.5067/6II6VW8LLWJ7)

Gillet-Chaulet F, Durand G, Gagliardini O, Mosbeux C, Mouginot J, Rémy F and Ritz C (2016) Assimilation of surface velocities acquired between 1996 and 2010 to constrain the form of the basal friction law under Pine Island Glacier. *Geophysical Research Letters*, **43**(19), 10–311

Glen J (1958) The flow law of ice: A discussion of the assumptions made in glacier theory, their experimental foundations and consequences. *IASH Publ*, **47**(171), e183

Goldsby D and Kohlstedt DL (2001) Superplastic deformation of ice: Experimental observations. *Journal of Geophysical Research: Solid Earth*, **106**(B6), 11017–11030 (doi: 10.1029/2000JB900336)

Gopalan G, Hrafnkelsson B, Aðalgeirsdóttir G and Pálsson F (2021) Bayesian inference of ice softness and basal sliding parameters at Langjökull. *Frontiers in Earth Science*, **9**, 610069 (doi: 10.3389/feart.2021.610069)

Habermann M, Truffer M and Maxwell D (2013) Changing basal conditions during the speed-up of Jakobshavn Isbræ, Greenland. *Cryosphere*, **7**(6)

Hensman J, Fusi N and Lawrence ND (2013) Gaussian processes for big data. *arXiv preprint arXiv:1309.6835* (doi: 10.48550/arXiv.1309.6835)

Huszár F (2015) How (not) to train your generative model: Scheduled sampling, likelihood, adversary? *arXiv preprint arXiv:1511.05101*

Isaac T, Petra N, Stadler G and Ghattas O (2015) Scalable and efficient algorithms for the propagation of uncertainty from data through inference to prediction for large-scale problems, with application to flow of the Antarctic ice sheet. *Journal of Computational Physics*, **296**, 348–368 (doi: 10.1016/j.jcp.2015.04.047)

Jansen D, Luckman A, Kulessa B, Holland PR and King EC (2013) Marine ice formation in a suture zone on the larsen c ice shelf and its influence on ice shelf dynamics. *Journal of Geophysical Research: Earth Surface*, **118**(3), 1628–1640 (doi: 10.1002/jgrf.20120)

Joughin I, Smith BE, Howat IM, Scambos T and Moon T (2010) Greenland flow variability from ice-sheet-wide velocity mapping. *Journal of Glaciology*, **56**(197), 415–430 (doi: 10.3189/002214310792447734)

Jouvet G, Cordonnier G, Kim B, Lüthi M, Vieli A and Aschwanden A (2021) Deep learning speeds up ice flow modelling by several orders of magnitude. *Journal of Glaciology*, 1–14 (doi: 10.1017/jog.2021.120)

Khazendar A, Rignot E and Larour E (2009) Roles of marine ice, rheology, and fracture in the flow and stability of the Brunt/Stancomb-Wills Ice Shelf. *Journal of Geophysical Research: Earth Surface*, **114**(F4) (doi: 10.1029/2008JF001124)

Khazendar A, Rignot E and Larour E (2011) Acceleration and spatial rheology of Larsen C ice shelf, Antarctic Peninsula. *Geophysical Research Letters*, **38**(9) (doi: 10.1029/2011GL046775)

Kingma DP and Welling M (2013) Auto-encoding variational bayes. *arXiv preprint arXiv:1312.6114*

Kulessa B, Jansen D, Luckman AJ, King EC and Sammonds PR (2014) Marine ice regulates the future stability of a large Antarctic ice shelf. *Nature communications*, **5**(1), 1–7 (doi: 10.1038/ncomms4707)

Larour E, Rignot E, Joughin I and Aubry D (2005) Rheology of the Ronne Ice Shelf, Antarctica, inferred from satellite radar interferometry data using an inverse control method. *Geophysical Research Letters*, **32**(5) (doi: 10.1029/2004GL021693)

Larour E, Rignot E, Poinelli M and Scheuchl B (2021) Physical processes controlling the rifting of Larsen C Ice Shelf, Antarctica, prior to the calving of iceberg A68. *Proceedings of the National Academy of Sciences*, **118**(40) (doi: 10.1073/pnas.2105080118)

LeCun Y, Kavukcuoglu K and Farabet C (2010) Convolutional networks and applications in vision. In *Proceedings of 2010 IEEE international symposium on circuits and systems*, 253–256, IEEE

Li Z, Kovachki NB, Azizzadenesheli K, Liu B, Bhattacharya K, Stuart AM and Anandkumar A (2020) Fourier neural operator for parametric partial differential equations. *CoRR*, **abs/2010.08895**

MacAyeal DR (1989) Large-scale ice flow over a viscous basal sediment: Theory and application to ice stream B, Antarctica. *Journal of Geophysical Research: Solid Earth*, **94**(B4), 4071–4087 (doi: 10.1029/JB094iB04p04071)

MacAyeal DR (1993) A tutorial on the use of control methods in ice-sheet modeling. *Journal of Glaciology*, **39**(131), 91–98

MacAyeal DR, Rignot E and Hulbe CL (1998) Ice-shelf dynamics near the front of the Filchner-Ronne Ice Shelf, Antarctica, revealed by SAR interferometry: model/interferogram comparison. *Journal of Glaciology*, **44**(147), 419–428

Matthews AGdG, Hensman J, Turner R and Ghahramani Z (2016) On sparse variational methods and the Kullback-Leibler divergence between stochastic processes. In *Artificial Intelligence and Statistics*, 231–239, PMLR

Millstein JD, Minchew BM and Pegler SS (2022) Ice viscosity is more sensitive to stress than commonly assumed. *Communications Earth & Environment*, **3**(1), 1–7 (doi: 10.1038/s43247-022-00385-x)

Mitcham T, Gudmundsson GH and Bamber JL (2022) The instantaneous impact of calving and thinning on the Larsen C Ice Shelf. *The Cryosphere*, **16**(3), 883–901 (doi: 10.5194/tc-16-883-2022)

Morlighem M, Rignot E, Seroussi H, Larour E, Ben Dhia H and Aubry D (2010) Spatial patterns of basal drag inferred using control methods from a full-stokes and simpler models for pine island glacier, west antarctica. *Geophysical Research Letters*, **37**(14)

Morlighem M, Williams CN, Rignot E, An L, Arndt JE, Bamber JL, Catania G, Chauché N, Dowdeswell JA, Dorschel B, Fenty I, Hogan K, Howat I, Hubbard A, Jakobsson M, Jordan TM, Kjeldsen KK, Millan R, Mayer L, Mouginot J, Noël BPY, O'Cofaigh C, Palmer S, Rysgaard S, Seroussi H, Siegert MJ, Slabon P, Straneo F, van den Broeke MR, Weinrebe W, Wood M and Zinglersen KB (2017) Bedmachine v3: Complete bed topography and ocean bathymetry mapping of Greenland from multibeam echo sounding combined with mass conservation. *Geophysical Research Letters*, **44**(21), 11051–11061 (doi: 10.1002/2017GL074954)

Morlighem M, Rignot E, Binder T, Blankenship D, Drews R, Eagles G, Eisen O, Ferraccioli F, Forsberg R, Fretwell P and others (2020) Deep glacial troughs and stabilizing ridges unveiled beneath the margins of the Antarctic ice sheet. *Nature Geoscience*, **13**(2), 132–137

Mouginot J, Scheuchl B and Rignot E (2012) Mapping of ice motion in Antarctica using synthetic-aperture radar data. *Remote Sensing*, **4**(9), 2753–2767, ISSN 2072-4292 (doi: 10.3390/rs4092753)

Mouginot J, Rignot E, Scheuchl B and Millan R (2017) Comprehensive annual ice sheet velocity mapping using Landsat-8, Sentinel-1, and RADARSAT-2 data. *Remote Sensing*, **9**(4), 364 (doi: 10.3390/rs9040364)

Nias IJ, Cornford SL, Edwards TL, Gourmelen N and Payne AJ (2019) Assessing uncertainty in the dynamical ice response to ocean warming in the Amundsen Sea Embayment, West Antarctica. *Geophysical Research Letters*, **46**(20), 11253–11260 (doi: 10.1029/2019GL084941)

Nick FM, Van der Veen CJ, Vieli A and Benn DI (2010) A physically based calving model applied to marine outlet glaciers and implications for the glacier dynamics. *Journal of Glaciology*, **56**(199), 781–794 (doi: 10.3189/002214310794457344)

Penny W, Kiebel S and Friston K (2007) Chapter 24 - variational bayes. In K FRISTON, J ASHBURNER, S KIEBEL, T NICHOLS and W PENNY (eds.), *Statistical Parametric Mapping*, 303–312, Academic Press, London, ISBN 978-0-12-372560-8 (doi: 10.1016/B978-012372560-8/50024-3)

Petra N, Martin J, Stadler G and Ghattas O (2014) A computational framework for infinite-dimensional bayesian inverse problems, part ii: Stochastic newton mcmc with application to ice sheet flow inverse problems. *SIAM Journal on Scientific Computing*, **36**(4), A1525–A1555 (doi: 10.1137/130934805)

Phan D, Pradhan N and Jankowiak M (2019) Composable effects for flexible and accelerated probabilistic programming in NumPyro. *arXiv preprint arXiv:1912.11554*

Pralong MR and Gudmundsson GH (2011) Bayesian estimation of basal conditions on Rutford Ice Stream, West Antarctica, from surface data. *Journal of Glaciology*, **57**(202), 315–324 (doi: 10.3189/002214311796406004)

Qi C and Goldsby DL (2021) An experimental investigation of the effect of grain size on “dislocation creep” of ice. *Journal of Geophysical Research: Solid Earth*, **126**(9), e2021JB021824 (doi: 10.1029/2021JB021824)

Raissi M, Yazdani A and Karniadakis GE (2020) Hidden fluid mechanics: Learning velocity and pressure fields from flow visualizations. *Science*, **367**(6481), 1026–1030 (doi: 10.1126/science.aaw4741)

Rasmussen CE (2003) Gaussian processes in machine learning. In *Summer school on machine learning*, 63–71, Springer

Reese R, Gudmundsson GH, Levermann A and Winkelmann R (2018) The far reach of ice-shelf thinning in Antarctica. *Nature Climate Change*, **8**(1), 53–57 (doi: 10.1038/s41558-017-0020-x)

Rezende D and Mohamed S (2015) Variational inference with normalizing flows. In *International conference on machine learning*, 1530–1538, PMLR

Riel B, Minchew B and Bischoff T (2021) Data-driven inference of the mechanics of slip along glacier beds using physics-informed neural networks: Case study on Rutford Ice Stream, Antarctica. *Journal of Advances in Modeling Earth Systems*, **13**(11), e2021MS002621 (doi: 10.1029/2021MS002621)

Rignot E, Mouginot J and Scheuchl B (2011) Ice flow of the Antarctic Ice Sheet. *Science*, **333**(6048), 1427–1430 (doi: 10.1126/science.1208336)

Schlegel NJ, Seroussi H, Schodlok MP, Larour EY, Boening C, Limonadi D, Watkins MM, Morlighem M and van den Broeke MR (2018) Exploration of Antarctic Ice Sheet 100-year contribution to sea level rise and associated model uncertainties using the ISSM framework. *The Cryosphere*, **12**(11), 3511–3534 (doi: 10.5194/tc-12-3511-2018)

Shapero DR, Badgeley JA, Hoffman AO and Joughin IR (2021) icepack: a new glacier flow modeling package in python, version 1.0. *Geoscientific Model Development*, **14**(7), 4593–4616 (doi: 10.5194/gmd-14-4593-2021)

Still H and Hulbe C (2021) Mechanics and dynamics of pinning points on the shirase coast, west antarctica. *The Cryosphere*, **15**(6), 2647–2665 (doi: 10.5194/tc-15-2647-2021)

Still H, Campbell A and Hulbe C (2019) Mechanical analysis of pinning points in the ross ice shelf, antarctica. *Annals of Glaciology*, **60**(78), 32–41 (doi: 10.1017/aog.2018.31)

Titsias M (2009) Variational learning of inducing variables in sparse gaussian processes. In *Artificial intelligence and statistics*, 567–574, PMLR

Tomczak J and Welling M (2018) Vae with a vampprior. In *International Conference on Artificial Intelligence and Statistics*, 1214–1223, PMLR